Quaternary Science Reviews 247 (2020) 106595

Contents lists available at ScienceDirect

Quaternary Science Reviews

journal homepage: www.elsevier.com/locate/quascirev

Post-LGM dynamic deglaciation along the Victoria Land coast, Antarctica

Hyun Hee Rhee [a, c], Min Kyung Lee [b], Yeong Bae Seong [a, *], Jae Il Lee [b], Kyu-Cheul Yoo [b], Byung Yong Yu [c]

[a] Department of Geography, Korea University, Seoul, 02841, South Korea
[b] Division of Polar Paleoenvironment, Korea Polar Research Institute, Incheon, 21990, South Korea
[c] AMS Laboratory, Korea Institute of Science and Technology, Seoul, 02792, South Korea

ARTICLE INFO

Article history:
Received 20 June 2020
Received in revised form
18 August 2020
Accepted 10 September 2020
Available online 29 September 2020

Keywords:
Antarctica
Terra Nova bay
Inexpressible island
Deglaciation
Cosmogenic exposure dating
Ross ice shelf

ABSTRACT

The post-Last Glacial Maximum (LGM) deglaciation of Antarctica holds important clues for understanding past environmental changes and predicting future changes in the Antarctic Ice Sheet. Cosmogenic nuclide exposure dating of glacial erratics documents the spatial and temporal glacier changes during the most recent deglaciation. We collected 55 erratic cobbles from the eight glaciated benches on Inexpressible Island, which is at the terminal area of Priestley Glacier, Terra Nova Bay, Victoria Land, to elucidate its post-LGM deglaciation pattern. Analyses of the ^{10}Be ages and ^{26}Al/^{10}Be ratios suggest that Priestley Glacier underwent ~254 m of lowering during the mid-Holocene, between 8.9 and 5.9 ka. This lowering rate (~0.09 m a^{-1}) is faster than those observed along other Victoria Land outlet glaciers to the north (Tucker and Aviator), but slower than the one to the south (Mackay). The post-LGM lowering of these outlet glaciers was triggered by marine ice sheet instability, with their asynchronous onsets of deglaciation derived from their diachronous response times to the southwestward migration of the grounding-line retreat until their synchronous termination of deglaciation at ~6 ka. A post-LGM deglaciation model with the southwestward migration of the western Ross Ice Shelf grounding line provides the best match to the terrestrial exposure dating results of the thinning patterns of the outlet glaciers along the Victoria Land coast.

1. Introduction

The ice sheets in Antarctica and Greenland are the only ones to survive the most recent glacial period, with an abundance of well-preserved evidence surrounding both ice sheets. Those evidences provide inferences on the responses of these two ice sheets to recent climatic changes and predicting future changes, particularly since these ice masses have the potential to make the greatest contribution to global sea-level rise under the current global warming trend (Shepherd, 2018, 2019). Global ice storages reached their maximum thickness or extent during the Last Glacial Maximum (LGM; 26.5–19 ka) with minimum sea level (Clark et al., 2009). Since then, the ice retreated and shrunk, leaving glacial sediments on the sea and the land from which many studies retrieved information on the environmental change over time (Bentley et al., 2009; Roberts et al., 2008).

The Ross Ice Shelf (RIS), which is the largest ice shelf in the world, drains both East Antarctic Ice Sheet (EAIS) and Western Antarctic Ice Sheet (WAIS) into the Ross Sea. Numerous outlet glaciers run out through the valleys along the Transantarctic Mountains (TAM) from EAIS, while WAIS directly flows with little landform obstacles. Deeper marine glacial sediments have been collected to retrieve clues on their depositional timing and associated environmental conditions via mineral grain, chemical composition, and biogenic species analyses, whereas ice-sheet geometry and modelling analyses have been conducted on the glacial landforms along continental shelves to determine their paleo-ice-flow directions (Golledge et al., 2014; Halberstadt et al., 2016). Marine studies have revealed the retreat history of the post-LGM grounding line and timing of the transition from a fully glaciated to an open-marine environment in the western Ross Sea via sediment core and bathymetry analyses (Halberstadt et al., 2016; McKay et al., 2016; Lee et al., 2017; Prothro et al., 2020).

* Corresponding author.
E-mail addresses: ybseong@korea.ac.kr, ybseong@gmail.com (Y.B. Seong).

https://doi.org/10.1016/j.quascirev.2020.106595
0277-3791/

Exposed ice-free areas on the TAM, between those valley outlet glaciers, contain the deglacial exposure histories of bedrock or sediments, which can be analyzed by *in situ* production of the cosmogenic nuclides and/or their decay. Various age dating analyses employing cosmogenic nuclides (e.g., ^{10}Be, ^{14}C, ^{21}Ne, ^{22}Ne, ^{26}Al) from glacial erratics and bedrock of terrestrial glacial landforms, and conventional organic ^{14}C from the biological components have provided information on ice thickness fluctuations and the timing of deglaciation. For example, terrestrial studies of erratics via cosmogenic nuclide exposure dating have revealed the post-LGM deglaciation histories of previously glaciated areas in Victoria Land, Antarctica (Jones et al., 2015; Goehring et al., 2019).

Here we document our terrestrial exposure dating results with both *in situ* ^{10}Be and ^{26}Al from Inexpressible Island and Priestley Glacier (Terra Nova Bay, Western Ross Sea; Fig. 1) erratics to reconstruct the ice thinning history. We compare them with other terrestrial erratic exposures, lowering rates, and offshore grounding-line retreat results. We then analyze the synthesized post-LGM deglaciation patterns along the Victoria Land coast using all of the available terrestrial exposure data and figure out the proper Ross Ice Shelf retreating pattern from several marine sediments or landform studies.

2. Study area

Priestley Glacier drains the southern area of Talos Dome, East Antarctic Ice Sheet (EAIS), and discharges its ice into Terra Nova Bay, Western Ross Sea (Fig. 1A). Priestly Glacier flows through a glacially scoured valley between the Deep Freeze and Eisenhower ranges and joins Reeves Glacier to form the Nansen Ice Shelf (Fig. 1B). Nansen Ice Shelf then merges into Drygalski Ice Tongue, which is the seaward extension of David Glacier and terminates in Terra Nova Bay. Our study area, Inexpressible Island, is at the present-day terminus of Priestley Glacier, which is located at the southern tip of the Northern Foothills. Inexpressible Island is one of the most historic places on Antarctica as a wintering base for some of the explorers of the British Antarctic Expedition. Priestley Glacier was named after a geologist Raymond E. Priestley, who first reported the raised beach on the island in the Northern Party of the expedition (Baroni and Orombelli, 1991).

The glacial landforms on Inexpressible Island can be divided into four broad morphological zones (Fig. 2C): (①) far-western cliffs; (②) mid-northern erratic mounds, (③) mid-southern terraces, and (④) eastern erratic-covered flats. Most of the surfaces are covered with erratic boulders or cobbles, with bedrock exposures found only on the far-western side of the island. The far-western side consists mainly of exposed bedrock (granite) cliffs with extremely steep slopes (Fig. 2C-①) and few erratics. The mid-northern part of the island has a series of convex mounds or flat benches, and concave slopes (Fig. 2C-②). These mounds or benches are mostly covered with erratic boulders of various lithologies; steep slopes exist between some of the mounds or benches, where erratics are unlikely to have been preserved stably. The mid-southern area has only a few flat and wide benches (i.e., terraces), with a high relief (>100 m) observed between benches (Fig. 2C-③). The eastern side of the island has very wide and flat benches with minor elevation variations (Fig. 2C-④). The benches on Inexpressible Island are mostly covered with erratic cobbles. Lateral moraines and raised beaches are present around Seaview Bay with keeping their palaeo marine limit (5.5 ± 0.5 ka BP, corrected ^{14}C age for reservoir effect of 1300 yr and CALIB 4.3) on 28 m asl (Fig. 2D; Berkman and Forman, 1996; Stuiver and Reimer, 2000; Baroni and Hall, 2004). Abundant cobbles and a few pebbles exist on the palaeo-beaches, whereas well-rounded pebbles are dominant on the present-day beaches.

3. Method

We used ^{10}Be and ^{26}Al in our exposure age dating and two-isotope analysis to determine whether the samples (or benches) were continuously (simply) exposed or not (Lal, 1991; Gosse and Phillips, 2001). Continuously exposed samples generally provide the most powerful and clearest evidence of glacier surface lowering. The difference between the two half-lives is not only suitable for detecting burial duration which is older than *ca.* 200 ka (Lal, 1991; Gosse and Phillips, 2001), but there is also the potential to detect continuous exposures of only *ca.* 50 ka (Lilly et al., 2010) to *ca.* 100 ka (Rhee et al., 2019).

A least-squared method (LSM) and Monte Carlo (MC) simulations in IceTEA were used for calculating the glacier lowering rate (Jones et al., 2019). The LSM determines the best-fit regression to the data, which minimizes the sum of the residuals, and the MC simulations produce probability distributions of glacier lowering via a series of simulation iterations. It would be proper to interpret the glacier lowering as constant and continuous when their MC ranges show tight results. A high correlation of linearity (R^2 value) between elevation and exposure ages will also explain the continuous lowering of glaciers, whereas low one would show complicated lowering phases.

3.1. Sampling strategy

We visited the glacial landforms from the northwestern upland to the southeastern shoreline of Inexpressible Island (Fig. 2C-②, ④, and 3) during the 2017−18 austral summer. The northern area has many flat and narrow mounds or benches that possess considerable topographic relief, with steep-slope surfaces between the benches (Fig. 3A and E). These steep surfaces could have been disturbed by the post-depositional mass movements, which might lead to either the pre-depositional inheritance of cosmogenic ^{10}Be and ^{26}Al, or post-depositional reworking. Samples were collected only on the gentle-slope, up-standing surfaces to minimize the reworking problem and partial shielding. Multiple cobble samples (>6) were collected at each bench to allow the removal of outliers from the statistical analyses. We also sampled the lowest bench (H), which was likely affected by palaeo-shoreline processes, to identify the upper limit of the raised beaches (Fig. 3C).

It is difficult to determine whether or not the boulders were exposed during glacial transportation. Supraglacial transportation makes the exposure age of a boulder older than the actual deglaciation time (inheritance). *In situ* shattered boulders and fragments can also introduce younger exposure ages (partial exposure or post-depositional reworking). Cobbles on low-standing surfaces are difficult to separate from boulder fragments, and they can also be partially shielded by the surrounding material, which may cause the younger-exposure-age problem (Heyman et al., 2011). Conversely, bullet-shaped cobbles are likely to be abraded during subglacial transportation. These abraded cobbles help avoid the inheritance problem and also minimize post-depositional alteration by removing the newly exposed fragments (Sugden et al., 2005; Balco and Schaefer, 2013; Jeong et al., 2018).

Therefore, samples evidencing sub-glacial abrasion were collected only on the gentle-slope, up-standing surfaces to minimize the possibility for inheritance due to supra-glacial transport and/or reworking and partial shielding after deposition. However, inheritance problems due to the incorporation of older drifts and multiple exposure inheritances (Di Nicola et al., 2009) may still exist. We also conducted a two-isotope analysis using isotopes with different half-lives to determine whether each sample possessed either a continuous exposure or multiple exposures, as well as a relative-probability analysis to screen out samples with old-

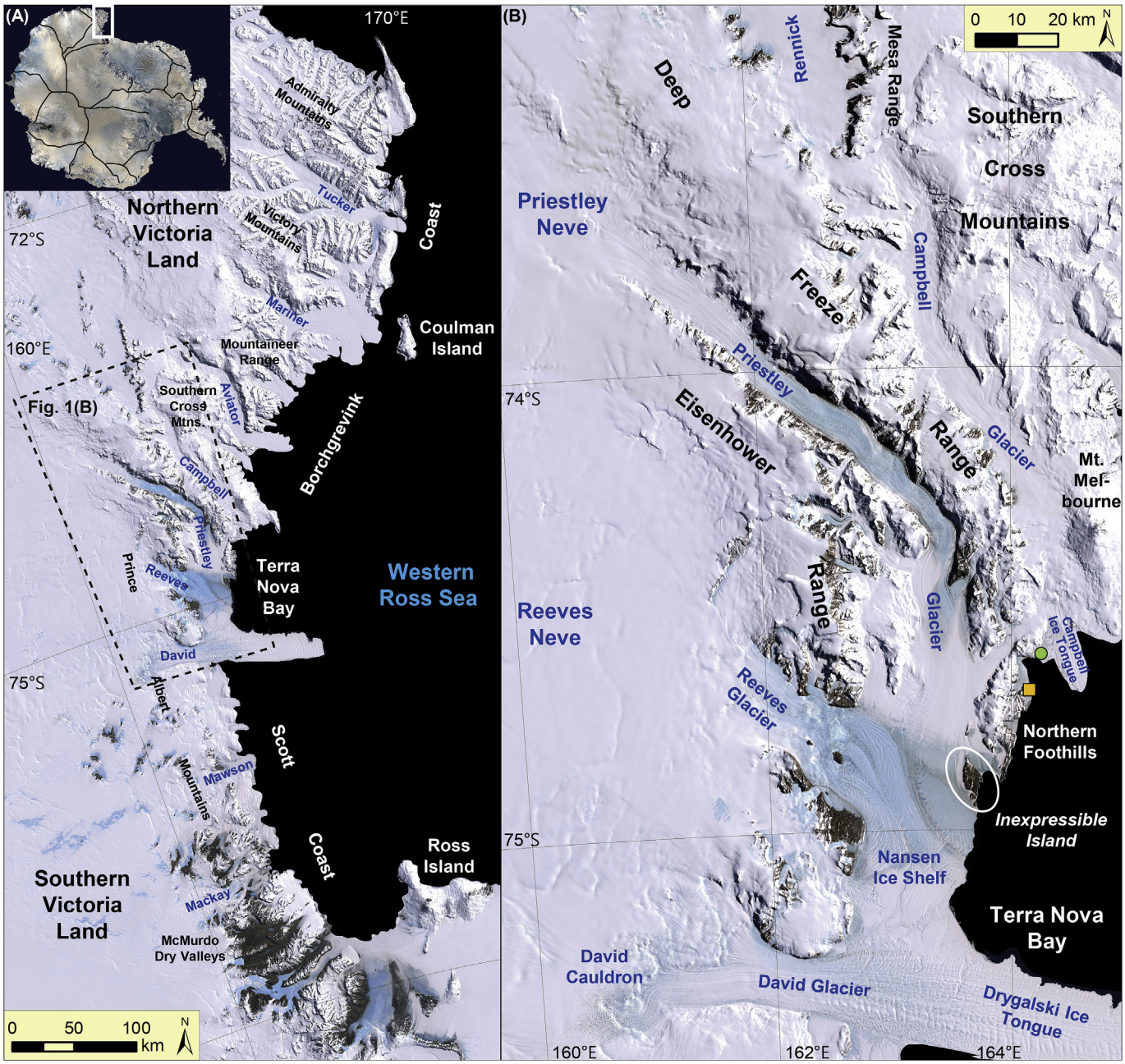

Fig. 1. Landsat Image Mosaic of Antarctica (LIMA) images of (A) Victoria Land and (B) Priestley Glacier. (A) The southern Victoria Land outlet glaciers drain ice from the East Antarctic Ice Sheet (EAIS) to the Scott Coast, and the northern Victoria Land outlet glaciers drain ice from the local mountain ranges to the Borchgrevink Coast. (B) The study area, Inexpressible Island, is at the present-day terminal margin of Priestley Glacier. The green circle indicates the location of Jangbogo Station (Korea), and the orange square indicates the location of Mario Zucchelli Station (Italy). (For interpretation of the references to color in this figure legend, the reader is referred to the Web version of this article.)

inheritance problem.

3.2. *In situ* ^{10}Be and ^{26}Al

The physical and chemical preparation of 55 erratic cobbles was undertaken at the Korea University Geochronology Laboratory, Seoul, as follows (Kohl and Nishiizumi, 1992; Seong et al., 2016). The entire samples were crushed using a jaw crusher and iron mortar to obtain medium-sized grains (250–500 μm). The resultant grains, which contained various minerals, were then leached in 1–3 %HF and HNO_3 to recover pure quartz, and to remove the other minerals and meteoric isotopes. Repeated leaching in a heating roller and ultrasonic bath aided further removal.

The pure quartz grains were mixed with a ^{9}Be carrier (1047.8 ppm ^{9}Be dissolved in HNO_3, 0.37–0.41 g at each sample) and dissolved in concentrated HF. The ^{10}Be within the grains came out to the mixture, which was mixed with ^{9}Be and ^{26}Al and ^{27}Al within the grains were also included in the solution. Aliquots were analyzed by inductively coupled plasma–atomic emission spectroscopy (ICP–AES) at the Korea Basic Science Institute, Seoul, to determine ^{27}Al concentrations. The samples were then fumed with $HClO_4$ to remove F and to prevent the formation of BeF_2, and HCl was used to form $BeCl_2$, which was suitable for the ion-exchange separation procedure. Beryllium was first extracted through the

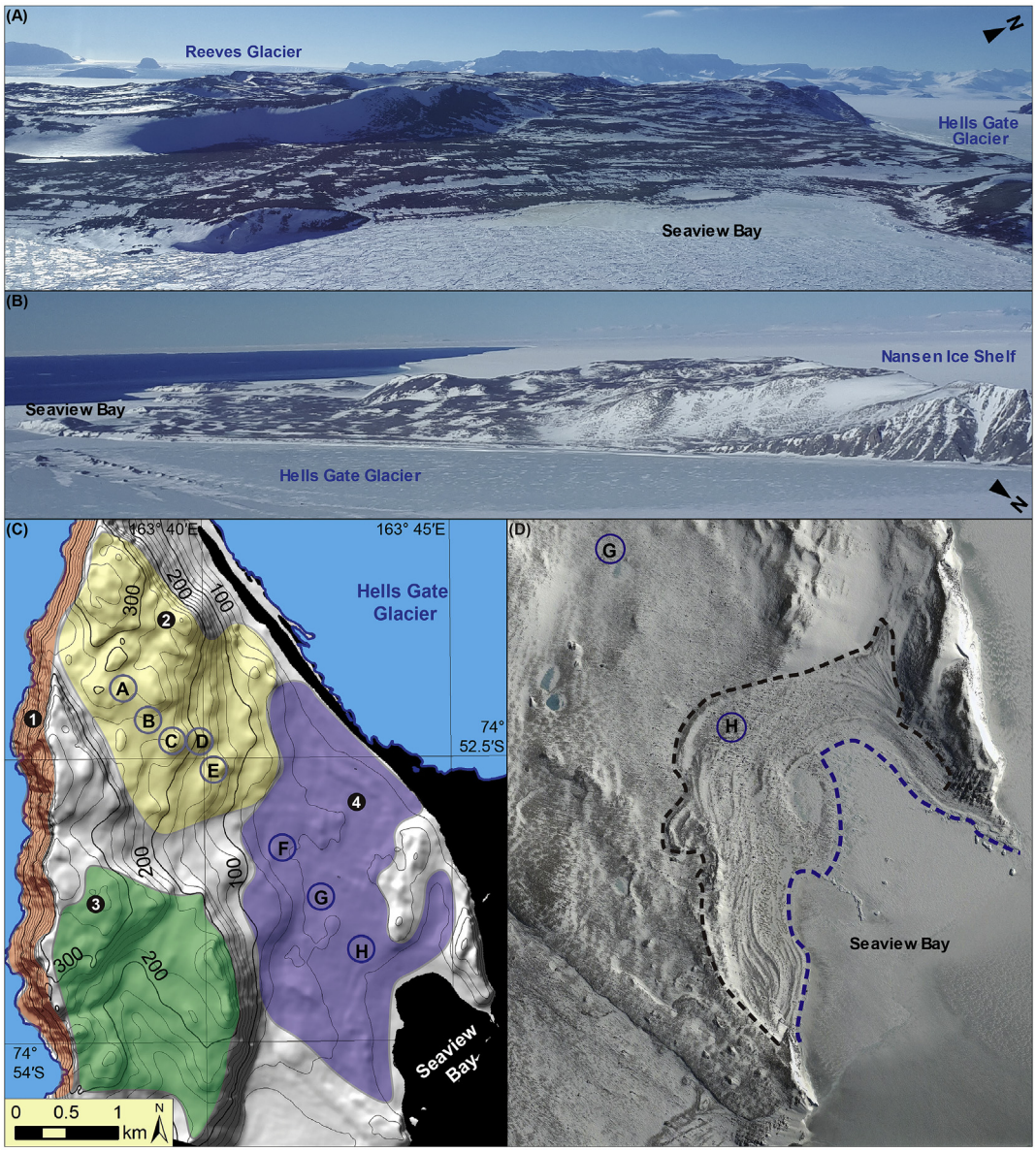

Fig. 2. Aerial photographs of the study area, taken from the (A) southeast and (B) northeast. (C) Hill-shaded topographic map of the study area, constructed from the Reference Elevation Model of Antarctica (REMA, 8-m resolution; Howat et al., 2019), with the eight sampled benches labeled A–H. The study area can be divided into four sectors based on the dominant landform type (① far-west: cliffs; ② mid-north: erratic mounds; ③ mid-south: terraces; ④ east: erratic-covered flats). (D) Satellite image of the coastal area of the study area. The dashed black line indicates the upper limit of the paleo-shoreline, and the dashed blue line marks the present-day shoreline. Bench H was initially formed by the past coastal processes, and then abandoned due to isostatic rebound (Baroni and Hall, 2004). (For interpretation of the references to color in this figure legend, the reader is referred to the Web version of this article.)

cation column before aluminum was eluted with concentrated HCl. The samples containing beryllium were neutralized with ammonia to obtain precipitated hydroxide gel. However, the samples with dissolved aluminum were temporally stored in polypropylene bottles, and only some of them were additionally treated and analyzed via accelerator mass spectrometry (AMS) for comparison with the beryllium results. Gels were washed with the Milli-Q water to remove ammonium salts, and the gels were dried in a crucible. The oxide form of each isotope was recovered via high-temperature calcination and then mixed with niobium and silver powder. The samples were pressed into aluminum or copper targets, and the subsequent AMS measurements were conducted at the Korea Institute of Science and Technology, Seoul.

The isotopic ratios were normalized using 07KNSTD 5–1 (2.709E-11 ± 1.073E-13) for Be and KNSTD 4–1 (7.444E-11 ± 5.119E-13) for Al (Nishiizumi et al., 2007). The stable isotope counts (^{9}Be, ^{27}Al) were calculated from the mass and concentration of the spiked ^{9}Be carrier and ^{27}Al concentration, determined by ICP–AES. The ^{10}Be and ^{26}Al counts were calculated from isotopic concentrations and ratios determined by AMS, with blank deductions (Tables 1–3). Exposure ages were calculated using the CRONUS-Earth online exposure age calculator v. 3.0 and scaling factor of LSDn (Balco et al., 2008; Lifton et al., 2014) and the IceTEA tool for two-isotope analysis (Jones et al., 2019).

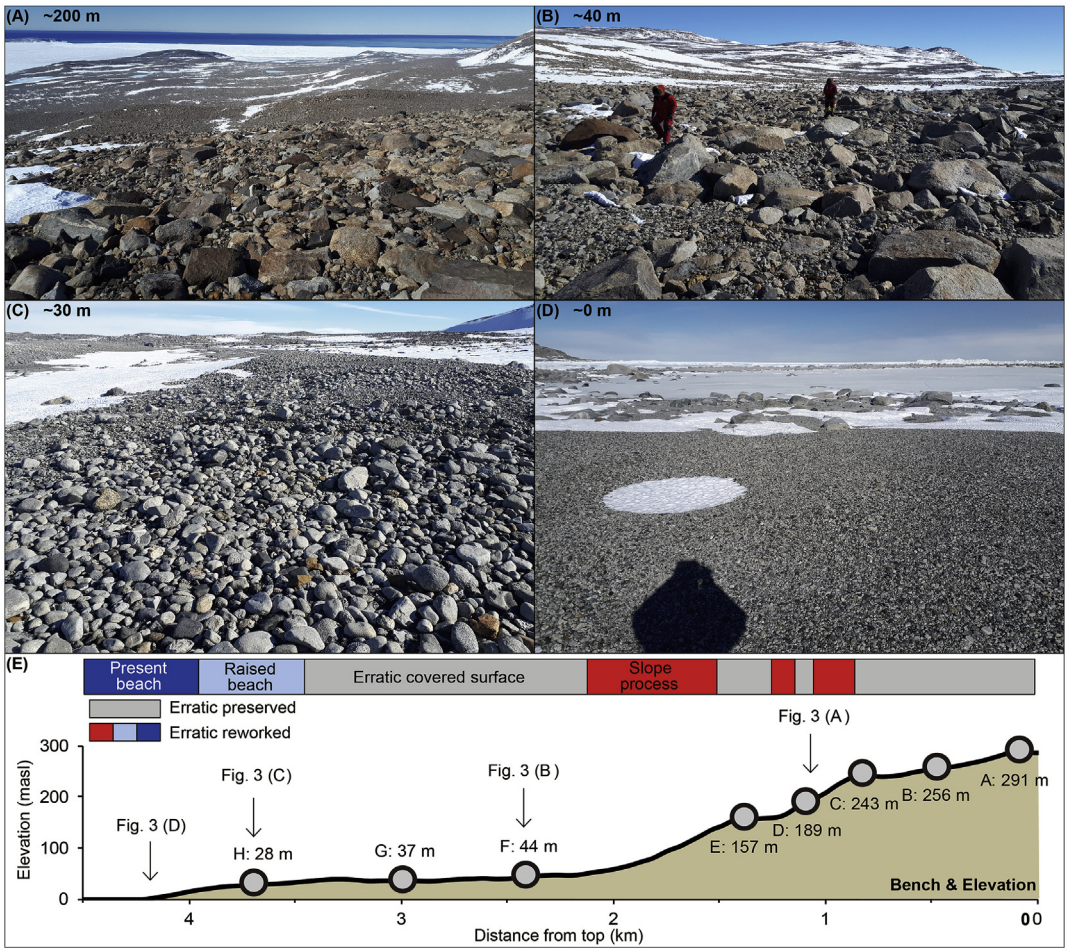

Fig. 3. Example photographs of the benches in the study area. (A) and (B) Erratics covering benches (A: ~200 m asl; B: ~40 m asl) that possess flat/gentle slopes, with a general increase in boulders toward the higher areas on each bench. The boulders may be mixed with shattered bedrock that was plucked via basal glacier movement in pressure-release areas. (C) The margin of the raised beach and erratic-covered zone in the study area. (D) The present-day beach at Seaview Bay. Boulders are rarely found in these low areas; the beaches are mostly covered with wave-eroded and well-rounded cobbles, as opposed to bullet-shaped erratic cobbles. All of the glacial erratic samples for the present study were collected above the present-day beach. (E) Longitudinal profile (NW–SE) of the study area, with the locations of the sample areas shown. The surfaces are described using different colors to indicate their predominant sedimentation patterns. They are covered mainly with erratics (gray), but several of the steep zones (red) and low-lying coastal zones (blue and sky blue) consisted of reworked deposits. (For interpretation of the references to color in this figure legend, the reader is referred to the Web version of this article.)

4. Results

All 55 samples had late Quaternary exposure ages in the three most recent interstadial periods (Marine Isotope Stage (MIS) 5, 3, and 1; Fig. 4A; Table 1). The five uppermost benches (benches A–E) had scattered MIS 7–1 ages. The samples had primarily MIS 1 ages, although many had MIS 5 ages, which highlighted the need to examine the possibility of multiple exposures via ^{26}Al analysis. The thirteen samples that were older than 50 ka (Lilly et al., 2010) underwent this additional ^{26}Al analysis. One sample (IEI053; 390.6 ± 26.2 ka) was excluded from this analysis and labeled an outlier due to its unreasonably old age. All of the >50 ka-old samples plotted in the multiple exposure (burial) zones of the two-isotope plot (Fig. 4B; Table 2). We therefore removed these samples as outliers, which allowed us to obtain more accurate effective exposure ages within a tighter range (<50 ka; MIS 3–1). Most of the samples on the lower three benches (benches F–H) were younger than 50 ka, except for four samples (IEI020, IEI011, IEI001, and IEI005). We treated all of the samples among the eight benches that were older than 50 ka as outliers and removed them from the analysis.

Two major peaks with kernel density estimates appeared with a similar probability of late MIS 3 ~ early MIS 2 and mid-MIS 1 exposure ages when all other <50 ka samples from all benches were included (Fig. 4C). These two peaks match the two most recent interstadial periods, but we favor the MIS 1 cluster for the following reasons. (1) The youngest samples are assigned as effective ages due to the higher risk of the inheritance during erratic cobble sampling (Owen et al., 2006; Di Nicola et al., 2009; Heyman et al., 2011). (2) The upper benches have the most abundant MIS 1 samples and lack MIS 3 samples (Fig. 4C). (3) The lower benches also exhibit much more loosely scattered ages with larger error ranges for the MIS 3 samples than the MIS 1 samples. (4) The kernel density plot across all of the benches has a higher and tighter cluster on MIS 1. (5) Samples at each bench also indicate a strong successive deglaciation pattern through MIS 1. (6) Finally, MIS 1 samples with both ^{26}Al and ^{10}Be measurements also show the simple exposure falling in the steady-state exposure island (Table 3; Fig. 4D). We therefore infer that the clustered MIS 3 samples were likely affected by inheritance from the upper area of the glacier or survived over-riding by ice during the previous glacial expansion (e.g. MIS 2).

These 16 simply exposed samples have mainly early-to mid-Holocene effective ages (10–5 ka), with the mean age at each bench

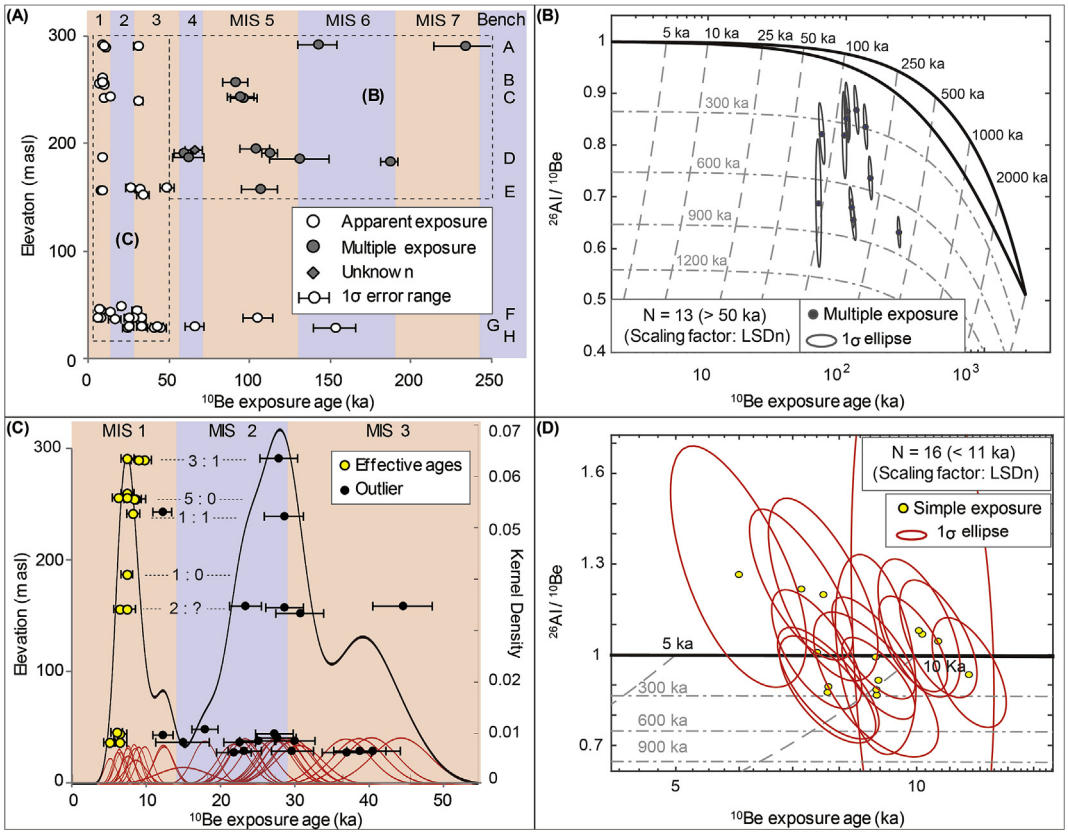

Fig. 4. (A) ^{10}Be age dating and (B) ^{26}Al/^{10}Be two-isotope analysis results. Samples older than 50 ka were excluded as multiply exposed or inheritance samples. (C) Kernel density plot of <50 ka samples. Two major peaks appeared on MIS 1 and MIS 3–2. Populations on the upper five benches (black values) show not only tightly concentrated, overwhelmingly abundant, and strongly successive samples falling into the MIS 1. (D) Additional ^{26}Al/^{10}Be two-isotope analysis results with MIS 1 samples. 1 σ error ranges of the whole MIS 1 samples (bold red ellipses) appeared crossing the steady-state exposure area (between black bold lines). These 16 samples results show the strongest evidence of MIS 1 simple and single lowering of a glacier. (For interpretation of the references to color in this figure legend, the reader is referred to the Web version of this article.)

falling within a tighter age range (8.9–5.9 ka; Table 3). We obtained the regression results with the mean age of simply exposed samples at each bench (Fig. 5A). The resultant lowering rate of Priestley Glacier is 0.089 m a^{-1} with a high coefficient of determination ($R^2 = 0.92$). This LSM-derived lowering rate is coincident with the MC simulation ranges, which have 1σ (0.083–0.118 m a^{-1}) and 2σ (0.073–0.147 m a^{-1}) ranges.

5. Discussion

5.1. Landscape evolution of Inexpressible Island

Two major geomorphic processes, glacier and beach processes, have shaped the two predominant landforms in the study area—glacial erratic-covered benches and raised beaches. The erratic-covered surfaces have previously been covered by flowing glaciers, with these erratics transported from either the upper drainage area or local bedrock fragmentation during glaciation, and subsequently exposed during glacier retreat and/or lowering. The raised beaches were affected by palaeo-shoreline processes, and have since been abandoned due to isostatic rebound (Baroni and Hall, 2004). Any erratics that are present on the raised beaches below the past marine limit cannot provide real exposure ages due to the reworking of the glacial deposits.

Our cosmogenic exposure samples of glacial erratics (Table 3) and ^{14}C dating of organic remains (Baroni and Hall, 2004) capture the successive evolution of both landforms in the study area (Figs. 5 and 6). The highest erratic-covered bench (291 m) on Inexpressible Island was first exposed at 8.9 ± 1.1 ka when the surface temperature on both west and east Antarctica already reached its maximum, induced from their isotopic studies (Parrenin et al., 2013; Cuffey et al., 2016). Priestley Glacier surface continued to lower until the last bench was exposed (37 m) at 5.9 ± 1.0 ka, which is coincident with the termination of the global sea-level rise (Lambeck et al., 2014). The ~254 m of lowering during this ~3.0-kyr time period continued with the highly lineated regression of lowering rate (Figs. 5A and 6A).

Seaview Bay first experienced open-marine conditions some time after 5.9 ± 1.0 ka, with the terminus of Priestley Glacier then becoming susceptible to open-ocean processes. These palaeo-shorelines were then abandoned due to isostatic rebound with the relative sea level (RSL) fall (Figs. 5B and 6B; Baroni and Hall, 2004). The residuals of on-land organics represent the maximum elevation or age boundary of palaeo-beaches, while marine organics show the minimum limits of them. RSL curve was drawn with their reservoir effect corrected ^{14}C age data (~1300 yr) and CALIB 4.3 from the Terra Nova Bay, and the onset of open-marine condition on the Seaview Bay (5.5 ± 0.5 ka, 28 m; Fig. 5B; Berkman and Forman, 1996; Stuiver and Reimer, 2000; Baroni and Hall, 2004) show successive landform evolution. We can therefore assume that the period between these proxies is marked by the termination of deglaciation, transition to an open-marine environment, and subsequent abandonment of the palaeo-shoreline (Fig. 6C).

Table 1
Results of ^{10}Be exposure age dating.

Name	Latitude	Longitude	Eleva-tion	Thick-ness[a]	Den-sity[b]	Shielding	Quartz	Be Carrier[d]	^{10}Be/^{9}Be[e,f]	^{10}Be Conc.[f,g]	Exposure
	(°S, DD)	(°E, DD)	(m asl)	(cm)	(g·cm^{-3})	Factor[c]	(g)	(g)	(10^{-13})	(10^{5} atoms·g^{-1})	Age[f,h] (ka)
Bench A											
IEI039	74.86866	163.63877	289.6	6.8	2.7	0.999961	35.8173	0.3809	0.9796 ± 0.0694	0.7025 ± 0.0530	10.05 ± 0.97
IEI040	74.86873	163.64007	291.1	9.4	3.0	0.999961	50.1994	0.4027	3.4855 ± 0.1303	1.9373 ± 0.0761	28.84 ± 2.06
IEI041	74.86891	163.63935	291.6	9.5	2.7	0.999961	49.6145	0.3913	0.9916 ± 0.0796	0.5276 ± 0.0448	7.68 ± 0.80
IEI042	74.86896	163.63848	290.7	7.2	2.7	0.999961	50.5214	0.3731	28.1490 ± 0.4181	14.5362 ± 0.2607	221.46 ± 14.44
IEI043	74.86922	163.63926	291.2	8.5	2.7	0.999961	50.9763	0.3828	17.0329 ± 0.3373	8.9365 ± 0.1988	134.66 ± 8.78
IEI044	74.86840	163.63969	290.4	7.4	2.7	0.999961	50.0554	0.4030	1.1720 ± 0.0859	0.6402 ± 0.0494	9.20 ± 0.90
Bench B											
IEI045	74.87168	163.64663	257.0	6.5	2.7	0.999689	51.3318	0.3724	11.2437 ± 0.2675	5.6929 ± 0.1475	86.23 ± 5.68
IEI046	74.87193	163.64752	255.1	6.2	2.7	0.999689	40.6530	0.3739	0.9629 ± 0.1353	0.5968 ± 0.0877	8.79 ± 1.39
IEI047	74.87182	163.64780	255.8	9.2	2.7	0.999689	52.4935	0.3956	0.8509 ± 0.0692	0.4299 ± 0.0374	6.52 ± 0.69
IEI048	74.87139	163.64691	260.3	6.3	2.7	0.999689	50.7037	0.3986	0.9959 ± 0.0682	0.5283 ± 0.0386	7.74 ± 0.73
IEI049	74.87194	163.64622	254.5	7	2.7	0.999689	42.0252	0.3861	0.9480 ± 0.0743	0.5865 ± 0.0488	8.70 ± 0.89
IEI050	74.87164	163.64580	256.6	7	2.7	0.999689	40.3356	0.3765	0.8256 ± 0.0634	0.5159 ± 0.0426	7.63 ± 0.78
Bench C											
IEI051	74.87392	163.65641	242.6	10.2	2.7	0.999871	44.6672	0.3812	9.6355 ± 0.2472	5.7359 ± 0.1587	90.87 ± 6.06
IEI052	74.87381	163.65716	242.5	8.5	2.7	0.999871	50.4171	0.3881	1.0805 ± 0.0678	0.5629 ± 0.0376	8.54 ± 0.76
IEI053	74.87422	163.65782	234.7	7.6	2.7	0.999871	50.0763	0.3851	43.1282 ± 0.4961	23.2026 ± 0.3540	390.61 ± 26.29
IEI054	74.87381	163.65807	239.3	7.6	2.7	0.999871	38.2428	0.3958	2.6970 ± 0.1241	1.9282 ± 0.0925	29.53 ± 2.26
IEI055	74.87345	163.65781	242.7	8.6	2.7	0.999871	43.1726	0.3777	9.3678 ± 0.2400	5.7160 ± 0.1580	89.36 ± 5.95
IEI056	74.87365	163.65665	243.8	8.7	2.7	0.999871	41.4764	0.3912	1.2922 ± 0.0850	0.8294 ± 0.0574	12.66 ± 1.16
Bench D											
IEI030	74.87375	163.66423	194.5	8	2.7	0.998666	49.2036	0.3810	11.0376 ± 0.2924	5.9645 ± 0.1696	97.63 ± 6.55
IEI031	74.87346	163.66490	193.5	7.5	3.0	0.998666	49.8208	0.3771	7.2030 ± 0.1780	3.7981 ± 0.1020	61.89 ± 4.07
IEI032	74.87366	163.66502	190.8	8	2.7	0.998666	40.6923	0.3732	5.3615 ± 0.1633	3.4195 ± 0.1107	55.58 ± 3.79
IEI033	74.87367	163.66593	186.8	9	2.7	0.998666	50.3602	0.3822	0.9316 ± 0.0704	0.4758 ± 0.0383	7.67 ± 0.77
IEI034	74.87328	163.66543	191.3	5.4	3.0	0.998666	49.6828	0.3821	12.1883 ± 0.3061	6.5436 ± 0.1775	106.02 ± 7.07
IEI035	74.87341	163.66626	187.0	8	2.7	0.998666	36.5498	0.3853	4.9107 ± 0.1666	3.5978 ± 0.1285	58.76 ± 4.11
IEI036	74.87369	163.66664	183.0	6	2.7	0.998666	49.6689	0.3863	19.5296 ± 1.0045	10.6151 ± 0.5573	176.45 ± 14.57
IEI037	74.87392	163.66546	185.3	7.5	2.7	0.998666	51.2621	0.3829	14.3336 ± 0.2912	7.4773 ± 0.1699	123.93 ± 8.08
Bench E											
IEI023	74.87524	163.66954	157.3	7	3.0	0.999308	49.8150	0.3813	11.0883 ± 0.3192	5.9231 ± 0.1812	100.52 ± 6.85
IEI024	74.87569	163.66850	158.7	7.8	2.7	0.999308	39.3881	0.3922	3.9780 ± 0.1481	2.7481 ± 0.1073	45.89 ± 3.28
IEI025	74.87568	163.66976	156.9	8	3.0	0.999308	50.1951	0.3988	3.1970 ± 0.1220	1.7583 ± 0.0705	29.54 ± 2.12
IEI026	74.87560	163.67063	155.8	11.7	2.7	0.999308	50.1258	0.3997	0.7416 ± 0.0703	0.3938 ± 0.0401	6.73 ± 0.79
IEI027	74.87673	163.67047	152.3	6.5	3.0	0.999308	50.5805	0.3746	3.6965 ± 0.2523	1.8980 ± 0.1324	31.64 ± 2.91
IEI028	74.87654	163.66953	158.1	6	2.7	0.999308	47.4675	0.3980	2.5432 ± 0.1040	1.4718 ± 0.0633	24.08 ± 1.77
IEI029	74.87639	163.67029	156.1	8	2.7	0.999308	40.7036	0.3730	0.7639 ± 0.0867	0.4669 ± 0.0564	7.69 ± 1.04
Bench F											
IEI016	74.88324	163.69538	39.9	7.5	2.7	0.999459	51.4867	0.3935	2.8662 ± 0.1377	1.5144 ± 0.0756	28.28 ± 2.20
IEI017	74.88259	163.69450	42.7	8.5	2.7	0.999459	45.5756	0.3923	1.1635 ± 0.0838	0.6794 ± 0.0515	12.67 ± 1.22
IEI018	74.88254	163.69364	43.6	7.5	2.7	0.999459	49.9937	0.3884	0.7056 ± 0.0641	0.3641 ± 0.0357	6.73 ± 0.77
IEI019	74.88290	163.69298	44.5	7	2.7	0.999459	48.2239	0.4063	2.5904 ± 0.1167	1.5067 ± 0.0709	27.91 ± 2.12
IEI020	74.88323	163.69179	47.2	8.5	2.7	0.999459	51.4864	0.3952	28.1036 ± 0.3852	15.0843 ± 0.2564	302.33 ± 20.04
IEI021	74.88256	163.69218	45.4	8.3	2.7	0.999459	50.2123	0.3789	0.6721 ± 0.0635	0.3360 ± 0.0344	6.25 ± 0.74
IEI022	74.88286	163.69116	47.9	7.5	2.7	0.999459	50.1699	0.3731	1.9459 ± 0.0983	0.9944 ± 0.0526	18.35 ± 1.46
Bench G											
IEI009	74.88730	163.70580	36.9	6	2.7	0.999538	52.9057	0.3982	0.7231 ± 0.0728	0.3620 ± 0.0391	6.65 ± 0.82
IEI010	74.88701	163.70355	37.0	9	2.7	0.999538	50.1697	0.4052	2.8966 ± 0.1303	1.6175 ± 0.0758	30.69 ± 2.33
IEI011	74.88676	163.70553	37.1	8	2.7	0.999538	45.3723	0.3803	8.7922 ± 0.2191	5.1386 ± 0.1388	98.51 ± 6.55
IEI012	74.88706	163.70446	36.9	9.5	2.7	0.999538	43.7036	0.3734	0.4967 ± 0.0605	0.2755 ± 0.0371	5.23 ± 0.77
IEI013	74.88740	163.70420	36.6	6.5	2.7	0.999538	52.0198	0.3731	1.6879 ± 0.3683	0.8294 ± 0.1853	15.33 ± 3.56
IEI014	74.88704	163.70664	37.2	8.5	2.7	0.999538	50.2090	0.3736	2.6450 ± 0.1349	1.3591 ± 0.0719	25.64 ± 2.05
IEI015	74.88644	163.70760	37.0	7	2.7	0.999538	50.1745	0.3774	2.4044 ± 0.1121	1.2472 ± 0.0607	23.23 ± 1.79
Bench H											
IEI001	74.89207	163.72452	29.2	6	2.7	0.999747	49.6147	0.3761	6.1988 ± 0.1765	3.2708 ± 0.0995	61.59 ± 4.15
IEI002	74.89223	163.72318	27.9	9	2.7	0.999747	50.7494	0.3924	3.6832 ± 0.1545	1.9744 ± 0.0862	37.88 ± 2.81
IEI003	74.89212	163.72270	27.9	8.5	2.7	0.999747	50.4927	0.3880	2.2195 ± 0.1399	1.1747 ± 0.0765	22.34 ± 1.97
IEI004	74.89208	163.72260	27.9	8.9	2.7	0.999747	50.5668	0.3844	4.0946 ± 0.1471	2.1601 ± 0.0815	41.46 ± 2.93
IEI005	74.89190	163.72193	28.2	4.9	3.0	0.999747	50.7762	0.3924	13.8382 ± 0.3034	7.4681 ± 0.1805	143.06 ± 9.46
IEI006	74.89195	163.71918	29.0	6.8	3.0	0.999747	50.0909	0.4006	2.2864 ± 0.1129	1.2600 ± 0.0649	23.76 ± 1.87
IEI007	74.89273	163.71593	28.7	6.1	3.0	0.999747	49.6345	0.3869	3.9001 ± 0.1558	2.1088 ± 0.0879	39.72 ± 2.90
IEI008	74.89278	163.71558	28.8	4.9	3.0	0.999747	51.1154	0.3935	3.0717 ± 0.1634	1.6361 ± 0.0899	30.40 ± 2.47

[a] Thickness of erratic cobbles.
[b] Densities of granite or quartzite (2.7 or 3.0 g cm^{-3}) were used.
[c] Factors for correcting geometric shielding measured at 10° intervals.
[d] Be carrier was spiked 0.37–0.41 g at each sample with containing 1047.8 ppm of ^{9}Be dissolved in HNO_3.
[e] The ^{10}Be/^{9}Be ratios were normalized using 07KNSTD reference sample 5–1 (2.709E-11 ± 1.073E-13) of Nishiizumi et al. (2007) and ^{10}Be half-life of 1.38E6 (Korschinek et al., 2010).
[f] Uncertainties are calculated at the 1σ confidence interval.
[g] A mean value of process blank samples (3.621E-15 ± 1.240E-15) was used for correction of background, and then divided into the mass of quartz.
[h] Ages were calculated assuming zero erosion and using CRONUS-Earth online calculator 3.0 of Balco et al. (2008) with scaling factors of LSDn (Lifton et al., 2014). Data are described in Fig. 4A.

Table 2
Results of ^{10}Be and ^{26}Al (>50 ka).

Name	Elevation (masl)	Be			Al			
		^{10}Be/^{9}Be[a,b]	^{10}Be Conc.	^{10}Be Exposure	^{26}Al/^{27}Al[b,d] (10^{-12})	^{27}Al Conc.[e]	^{26}Al Conc.	^{26}Al/^{10}Be[f]
		(10^{-13})	(10^{5} atoms g^{-1})	Age[c] (ka)		(10^{18} atoms g^{-1})	(10^{6} atoms g^{-1})	
Bench A								
IEI042	290.7	28.1490 ± 0.4181	14.5362 ± 0.2607	221.46 ± 14.44	4.6517 ± 0.1333	1.4357 ± 0.0099	6.6784 ± 0.1974	4.59 ± 0.15
IEI043	291.2	17.0329 ± 0.3373	8.9365 ± 0.1988	134.66 ± 8.78	3.4583 ± 0.1162	1.3837 ± 0.0177	4.7854 ± 0.1661	5.35 ± 0.22
Bench B								
IEI045	257.0	11.2437 ± 0.2675	5.6929 ± 0.1475	86.23 ± 5.68	0.9233 ± 0.0608	3.6736 ± 0.0143	3.3918 ± 0.2261	5.95 ± 0.42
Bench C								
IEI051	242.6	9.6355 ± 0.2472	5.7359 ± 0.1587	90.87 ± 6.06	6.9365 ± 0.2344	0.5205 ± 0.0066	3.6108 ± 0.1342	6.29 ± 0.29
IEI055	242.7	9.3678 ± 0.2400	5.7160 ± 0.1580	89.36 ± 5.95	4.5378 ± 0.1174	0.7805 ± 0.0070	3.5417 ± 0.0979	6.19 ± 0.24
Bench D								
IEI030	194.5	11.0376 ± 0.2924	5.9645 ± 0.1696	97.63 ± 6.55	3.9598 ± 0.1134	0.7452 ± 0.0065	2.9508 ± 0.0898	4.94 ± 0.20
IEI031	193.5	7.2030 ± 0.1780	3.7981 ± 0.1020	61.89 ± 4.07	1.6906 ± 0.0753	1.7603 ± 0.0942	2.9759 ± 0.1360	7.85 ± 0.40
IEI032	190.8	5.3615 ± 0.1633	3.4195 ± 0.1107	55.58 ± 3.79	0.2677 ± 0.0328	6.3957 ± 0.0115	1.7118 ± 0.2115	5.00 ± 0.63
IEI034	191.3	12.1883 ± 0.3061	6.5436 ± 0.1775	106.02 ± 7.07	5.0133 ± 0.1251	0.8246 ± 0.0166	4.1340 ± 0.1090	6.31 ± 0.23
IEI035	187.0	4.9107 ± 0.1666	3.5978 ± 0.1285	58.76 ± 4.11	2.6582 ± 0.0941	0.8095 ± 0.0095	2.1518 ± 0.0821	5.98 ± 0.31
IEI036	183.0	19.5296 ± 1.0045	10.6151 ± 0.5573	176.45 ± 14.57	0.1769 ± 0.0258	13.4581 ± 0.0996	2.3802 ± 0.3484	2.24 ± 0.34
IEI037	185.3	14.3336 ± 0.2912	7.4773 ± 0.1699	123.93 ± 8.08	4.3849 ± 0.1189	1.0369 ± 0.0057	4.5468 ± 0.1286	6.08 ± 0.22
Bench E								
IEI023	157.3	11.0883 ± 0.3192	5.9231 ± 0.1812	100.52 ± 6.85	4.2591 ± 0.1192	0.6640 ± 0.0104	2.8280 ± 0.0847	4.77 ± 0.20

[a] Ratios of ^{10}Be/^{9}Be were normalized with 07KNSTD reference sample 5−1 (2.709E-11 ± 1.073E-13) of Nishiizumi et al. (2007) and ^{10}Be half-life of 1.38E6 (Korschinek et al., 2010).
[b] Uncertainties were calculated at the 1σ confidence interval.
[c] Ages were calculated assuming zero erosion using the CRONUS-Earth online calculator 3.0 of Balco et al. (2008) and the scaling factor of LSDn (Lifton et al., 2014).
[d] Ratios of ^{26}Al/^{27}Al were normalized with KNSTD reference sample 4−1 (7.444E-11 ± 5.119E-13) of Nishiizumi et al. (2007).
[e] Concentration of ^{27}Al was measured with ICP-AES from a quartz dissolution aliquot.
[f] ^{26}Al/^{10}Be ratio and 1σ error range of each sample were checked for finding multiple exposures with a two-isotope plot in Fig. 4B.

Table 3
Results of ^{10}Be and ^{26}Al (<11 ka) and effective ages for the lowering of Priestley Glacier on Inexpressible Island.

Name	Elevation (masl)	Be[a]				Al[a]						Mean ^{10}Be age (ka)
		Quartz[a] (g)	^{10}Be/^{9}Be[b,c] (10^{-13})	^{10}Be Conc. (10^{5} atoms g^{-1})	^{10}Be Exposure Age[d] (ka)	Quartz[a] (g)	^{26}Al/^{27}Al[c,e] (10^{-13})	^{27}Al Conc.[f] (10^{18} atoms g^{-1})	^{26}Al Conc.[g] (10^{5} atoms g^{-1})	^{26}Al/^{10}Be[h]		
Bench A												
IEI039	289.6	35.8173	0.9796 ± 0.0694	0.7025 ± 0.0530	10.05 ± 0.97	39.1976	1.6190 ± 0.1857	2.9497 ± 0.0407	4.8073 ± 0.5514	6.84 ± 0.93		
IEI041	291.6	49.6145	0.9916 ± 0.0796	0.5276 ± 0.0448	7.68 ± 0.80	49.9450	6.8288 ± 0.6443	0.4870 ± 0.0013	3.6311 ± 0.3426	6.88 ± 0.87		
IEI044	290.4	50.0554	1.1720 ± 0.0859	0.6402 ± 0.0494	9.20 ± 0.90	40.5075	2.1009 ± 0.2170	2.3170 ± 0.0100	4.9374 ± 0.5102	7.71 ± 0.99	***8.98 ± 1.20***	
Bench B												
IEI046	255.1	40.6530	0.9629 ± 0.1353	0.5968 ± 0.0877	8.79 ± 1.39	51.1680	0.0617 ± 0.0436	75.1883 ± 1.0526	3.0397 ± 2.1494	5.09 ± 3.67		
IEI047	255.8	52.4935	0.8509 ± 0.0692	0.4299 ± 0.0374	6.52 ± 0.69	44.9536	2.1502 ± 0.2098	1.4671 ± 0.0114	3.2330 ± 0.3155	7.52 ± 0.98		
IEI048	260.3	50.7037	0.9959 ± 0.0682	0.5283 ± 0.0386	7.74 ± 0.73	38.2132	3.8386 ± 0.2770	0.9172 ± 0.0098	3.7328 ± 0.2694	7.06 ± 0.72		
IEI049	254.5	42.0252	0.9480 ± 0.0743	0.5865 ± 0.0488	8.70 ± 0.89	50.5691	1.2826 ± 0.1586	3.5942 ± 0.0248	4.5912 ± 0.5680	7.82 ± 1.16		
IEI050	256.6	40.3356	0.8256 ± 0.0634	0.5159 ± 0.0426	7.63 ± 0.78	47.6069	3.7415 ± 0.2973	1.0173 ± 0.0150	3.9656 ± 0.3152	7.68 ± 0.88	***7.87 ± 0.93***	
Bench C												
IEI052	242.5	50.4171	1.0805 ± 0.0678	0.5629 ± 0.0376	8.54 ± 0.76	48.9075	4.5685 ± 0.3638	0.9233 ± 0.0058	4.4138 ± 0.3515	7.84 ± 0.81	***8.54 ± 0.76***	
Bench D												
IEI033	186.8	50.3602	0.9316 ± 0.0704	0.4758 ± 0.0383	7.67 ± 0.77	50.7462	0.5467 ± 0.1183	6.2929 ± 0.0711	3.3307 ± 0.7211	7.00 ± 1.61	***7.67 ± 0.77***	
Bench E												
IEI026	155.8	50.1258	0.7416 ± 0.0703	0.3938 ± 0.0401	6.73 ± 0.79	41.7079	1.9948 ± 0.2015	1.2874 ± 0.0081	2.6502 ± 0.2677	6.72 ± 0.96		
IEI029	156.1	40.7036	0.7639 ± 0.0867	0.4669 ± 0.0564	7.69 ± 1.04	22.8564	1.2511 ± 0.1687	2.4062 ± 0.0130	3.0840 ± 0.4158	6.60 ± 1.19	***7.21 ± 0.68***	
Bench F												
IEI018	43.6	49.9937	0.7056 ± 0.0641	0.3641 ± 0.0357	6.73 ± 0.77	39.3376	2.1288 ± 0.2215	1.0927 ± 0.0119	2.4271 ± 0.2526	6.66 ± 0.95		
IEI021	45.4	50.2123	0.6721 ± 0.0635	0.3360 ± 0.0344	6.25 ± 0.74	45.3255	2.8139 ± 0.2720	1.0605 ± 0.0145	3.1043 ± 0.3001	9.24 ± 1.30	***6.49 ± 0.34***	
Bench G												
IEI009	36.9	52.9057	0.7231 ± 0.0728	0.3620 ± 0.0391	6.65 ± 0.82	44.9797	1.5016 ± 0.2012	2.1090 ± 0.0072	3.1982 ± 0.4287	8.83 ± 1.52		
IEI012	36.9	43.7036	0.4967 ± 0.0605	0.2755 ± 0.0371	5.23 ± 0.77	44.8255	1.0167 ± 0.1710	2.5027 ± 0.0078	2.5427 ± 0.4278	9.22 ± 1.98	***5.94 ± 1.01***	

[a] Al chemical treatment of MIS 1 samples was separately proceeded after the Be analysis with an aliquot of homogeneous quartz samples.
[b] Ratios of ^{10}Be/^{9}Be were normalized with 07KNSTD reference sample 5−1 (2.709E-11 ± 1.073E-13) of Nishiizumi et al. (2007) and ^{10}Be half-life of 1.38E6 (Korschinek et al., 2010).
[c] Uncertainties were calculated at the 1σ confidence interval.
[d] Ages were calculated assuming zero erosion using the CRONUS-Earth online calculator 3.0 of Balco et al. (2008) and the scaling factor of LSDn (Lifton et al., 2014).
[e] Ratios of ^{26}Al/^{27}Al were normalized with KNSTD reference sample 4−1 (7.444E-11 ± 3.921E-13) of Nishiizumi et al. (2007).
[f] Concentration of ^{27}Al was measured with ICP-AES from quartz dissolution aliquot.
[g] A mean value of process blank samples (2.131E-15 ± 8.513E-16) was used for correction of background.
[h] ^{26}Al/^{10}Be ratio and 1σ error range of each sample were checked for finding steady-state exposure with a two-isotope plot in Fig. 4D.

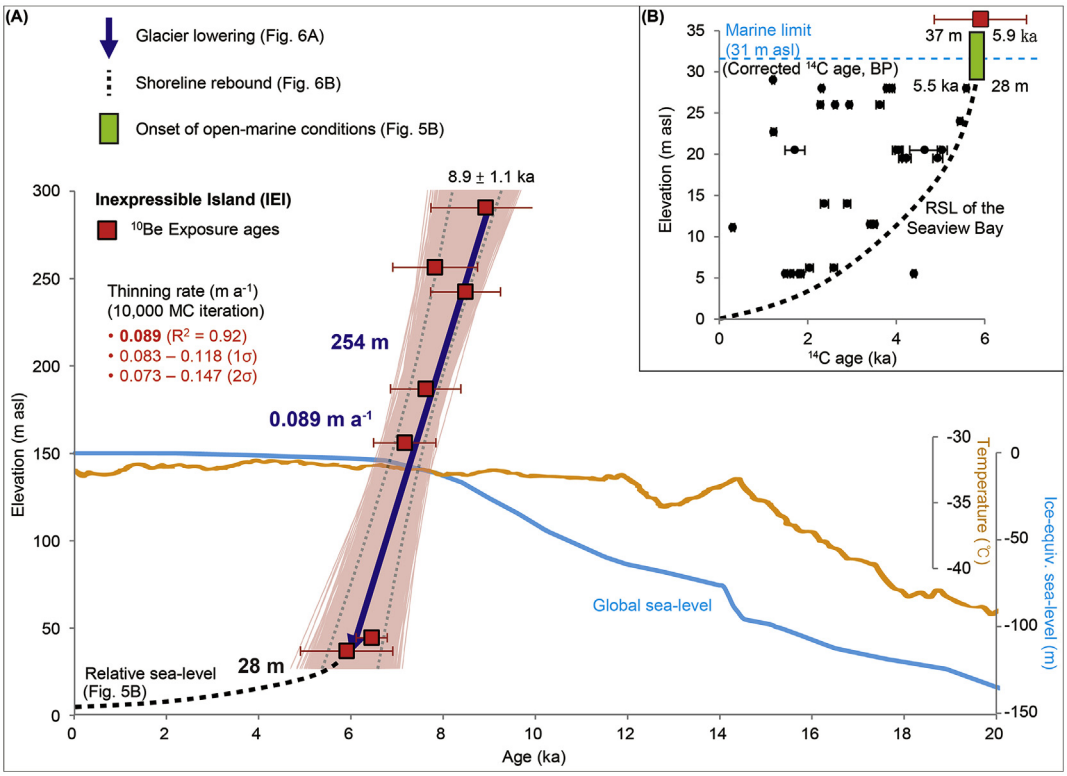

Fig. 5. (A) The red squares with red bars represent the mean ages at Inexpressible Island (IEI; Priestley Glacier) and their 1σ error range (Table 3). The red regions are the simulated lowering rates determined via a Monte Carlo simulation with 10,000 iterations using IceTEA (Jones et al., 2019). Dotted gray lines are the 1σ error ranges of the regression lines. A high correlation value between elevation and age was yielded ($R^2 = 0.92$), which means the lowering occurred continuously in high probability. Black dots and black dashed curves were redrawn with only SvB organic remains ^{14}C age samples (modified from Baroni and Hall, 2004). Both changes in the surface temperature (orange curve; Cuffey et al., 2016) and the eustatic sea-level rise (Lambeck et al., 2014; Goehring et al., 2019) seem to have little effect on our deglaciation result. However, the IEI switched to open-marine condition at ~6 ka, when both deglaciation and eustatic sea-level rise ended, and the relative sea-level fall began (green box). (For interpretation of the references to color in this figure legend, the reader is referred to the Web version of this article.)

5.2. Vertical changes in the Victoria Land outlet glaciers

Various outlet glaciers drain Victoria Land, with flow initiating mainly near Dome Charlie (Dome C) and Talos Dome in the EAIS and terminating in the western Ross Sea (Frezzotti et al., 2000; Rignot et al., 2011). Some of these outlet glaciers have been studied using cosmogenic surface exposure dating methods (Figs. 7 and 8; Jones et al., 2015; Rhee et al., 2019; Goehring et al., 2019). We compared our results with these previous studies to identify a plausible mechanism to trigger deglaciation in Victoria Land (Rignot et al., 2011; Goehring et al., 2019). Many forcings, such as temperature changes, sea-level rise, and ice-sheet bed instabilities have previously been discussed and compared. However, Campbell Glacier was generally excluded since it is isolated by the extremely high relief of the surrounding mountains, has a limited source area, and evolved in a unique environment compared to the adjacent outlet glaciers (Fig. 7; Orombelli, 1989; Di Nicola et al., 2009; Rhee et al., 2019).

Mackay Glacier is at the southernmost part of the present-day open-marine extent of the Ross Sea, draining into McMurdo Sound (Fig. 8-①). Its post-LGM deglaciation history can be divided into four phases (Jones et al., 2015). (1) The glacier sustained its surface level at ~260 m above the modern ice level until the LGM (~22 ka). (2) It was then lowered by ~30 m between the LGM and ~8 ka. (3) Mackay Glacier abruptly and rapidly collapsed between 6.8 and 6.0 ka, with ~200 m of glacier lowering recorded at an estimated lowering rate on 0.331–0.802 m yr^{-1}. (4) Another 25+ m of glacier lowering occurred from 6.0 ka until 250 years ago. The third phase, which occurred between 6.8 and 6.0 ka, was the major deglaciation period in this area. However, none of the climatic forcings, such as air temperature, sea surface temperature, and/or sea-level changes can fully account for this rapid lowering. The basal geomorphology along the topographic flowline profiles may likely explain this rapid lowering, with the over-deepened trough and reversed bed slope creating marine ice-sheet instability that led to this rapid collapse (Fig. 7-①; Jones et al., 2015; Lee et al., 2017).

The other glaciers in northern Victoria Land suggest that eustatic sea-level rise (ESL) was the dominant force that triggered the deglaciation of these outlet glaciers. (Fig. 8-③, ④; Goehring et al., 2019). The Tucker and Aviator glaciers drain northern Victoria Land and are also fed by local glaciers or neve as they flow toward the Ross Sea. Both glaciers were at least ~300 m thicker than their present-day glacier surfaces during the LGM. Major glacier lowering occurred between 17.2 ka and 5.1 ka on Tucker Glacier, and between 11.4 ka and 7.2 ka on Aviator Glacier. Their linear thinning phases were compared with both atmospheric and ocean temperature changes, but their maximum changes occurred at different times and rates. The temperature had already reached its maximum much earlier than the onset of deglaciation, and sea-level rise with grounding line retreat affected the deglaciation greater than the temperature increase during the Late Glacial (Cuffey et al., 2016). Eustatic sea-level rise during the Late Glacial period and early Holocene most corresponds with the linear lowering of these two glaciers. The grounding line retreat of both glaciers also passed through the reversed bedform, though their

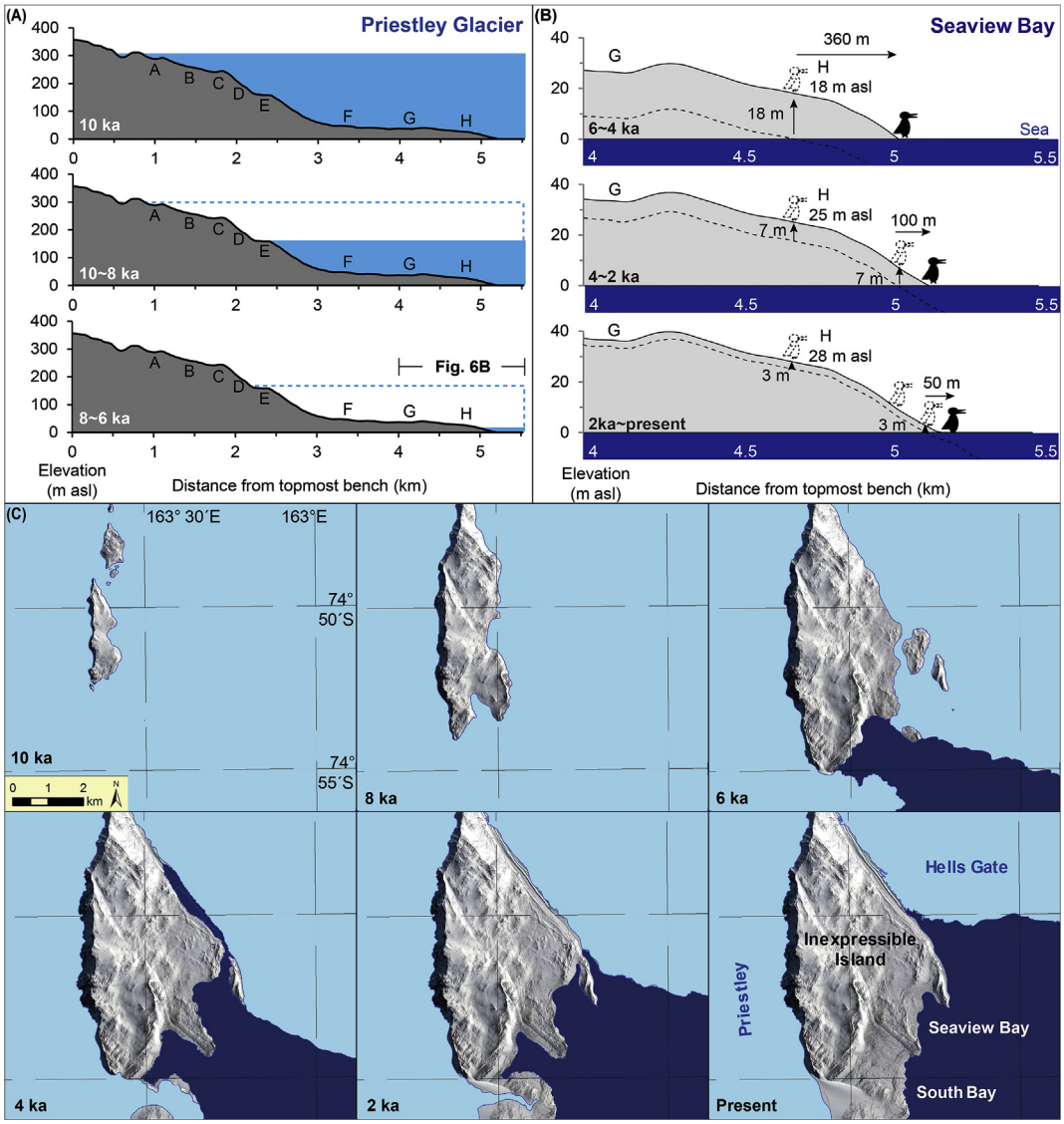

Fig. 6. Spatial changes in Priestley Glacier on Inexpressible Island throughout the Holocene. Extremely fast glacier lowering terminated at *ca.* 6 ka, which is connected with the end of eustatic sea-level rise and the onset of open-water conditions in Seaview Bay. (A) Modeled ice extent (sky blue) relative to the sampled benches. (B) A rebound of the raised beach since 6 ka. A dotted penguin is the position of past rookeries (raised beach) and black-filled one is the position of present rookeries (present beach). (C) Modeled ice extent (sky blue) and marine extent (dark blue) around Inexpressible Island throughout the Holocene (This study; Baroni and Hall, 2004). (For interpretation of the references to color in this figure legend, the reader is referred to the Web version of this article.)

lowering pattern occurred continuously and steady, unlike the southern glacier collapses (Fig. 7-③, ④).

Our Priestley Glacier results suggest that it experienced more rapid constant lowering than those observed along the other northern Victoria Land glaciers, but slower than southern Victoria Land glaciers (Fig. 8-②). The flanks of Inexpressible Island were covered by at least 300 m of ice during the LGM, which continued until *ca.* 10 ka. Major deglaciation then occurred during the early-to mid-Holocene (8.9–5.9 ka), resulting in ~254 m of glacier lowering (Fig. 5A). This period is later than the timing of deglaciation along the northern glaciers, but earlier than the timing of deglaciation along the southern glacier (Fig. 8). A southern glacier (Mackay) was rapidly collapsed by reversed bed instability during mid-Holocene, while steady deglaciation of the two northern glaciers (Tucker and Aviator) was likely driven by ESL rise through the Late glacial (20–16 ka) and the early Holocene. Priestley glacier lowered during the mid-Holocene like the southern glacier, but it took a relatively longer period (~3 kyr) unlike the rapid collapse. In contrast, the 3 kyr lowering has a similar constant lowering pattern with the northern glaciers, but it took relatively shorter period and commenced much later.

We therefore suggest that the Priestley glacier lowered down due to the complex conditions changes, which is related to the retreat of the Ross Ice Shelf grounding line. Priestley glacier already experienced all the deglaciation triggers, reversed bed ice instabilities (Fig. 7-②), ice buttressing with sea-level rise, and increased temperature (Fig. 8-②). But its lowering pattern or period suggests that Priestly glacier responded differently from both northern and southern glaciers. The spatial-temporal differences of deglaciations among the outlet glaciers are likely to be caused by the migrated grounding line retreat of the Ross Ice Shelf (Discussion 5.3). Furthermore, all the deglaciations terminated at around 6 ka for all of the Victoria Land outlet glaciers, coincident with the end of global sea-level rise when grounding lines of outlet glaciers

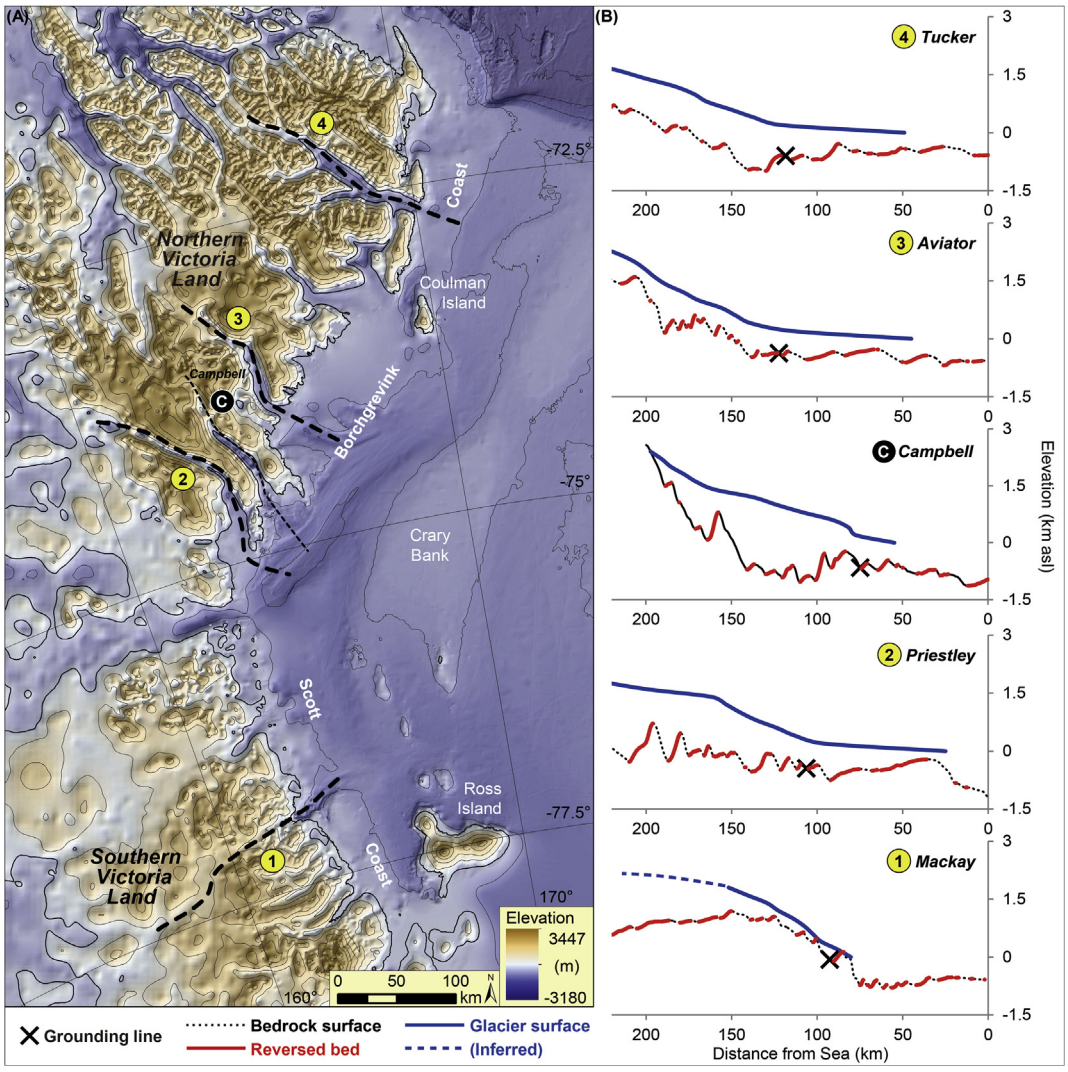

Fig. 7. Comparison of the topography of the marine bedforms along five Victoria Land outlet glaciers. (A) Topographic map of the margin between Victoria Land and the western Ross Sea. Campbell Glacier (©) is excluded because it is an isolated local glacier that is not connected to interior domes of the East Antarctic Ice Sheet; it is only fed by small local valley glaciers due to the extremely high relief of the surrounding mountains (Orombelli, 1989; Di Nicola et al., 2009; Rhee et al., 2019). (B) Comparison of the longitudinal profiles of the glacier and bedrock surfaces for each of the outlet glaciers (along the dashed black lines in (A)), with the present-day grounding line positions marked by the "X" symbol. A modelling study has suggested that Mackay Glacier (①) collapsed due to its reversed slope bed (red bold lines), whereas the other glaciers, which also have similar bedforms, underwent slower, steadier lowering (Jones et al., 2015). (For interpretation of the references to color in this figure legend, the reader is referred to the Web version of this article.)

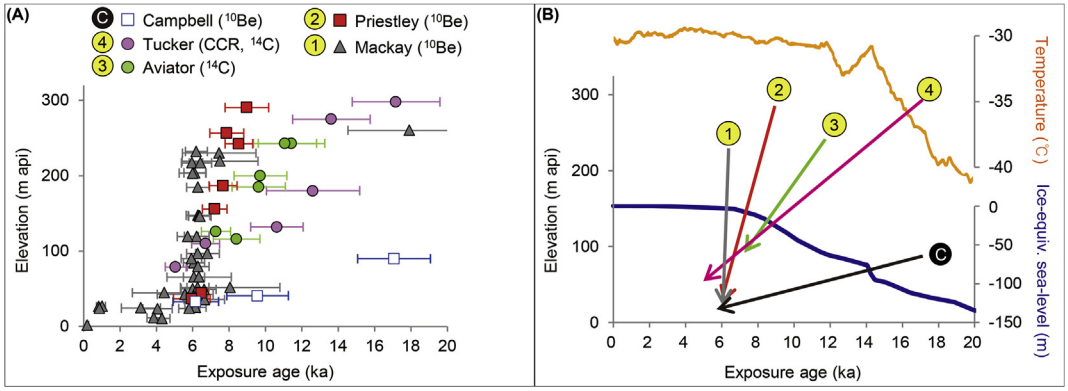

Fig. 8. (A) Compiled exposure ages across the Victoria Land coast via cosmogenic nuclide dating (① Jones et al., 2015; ② this study; ③ & ④ Goehring et al., 2019. CCR: Crater Cirque; © Rhee et al., 2019). (B) Linear lowering of the outlet glaciers, temperature fluctuations (Cuffey et al., 2016, and sea-level change (Lambeck et al., 2014) since the LGM in Victoria Land.

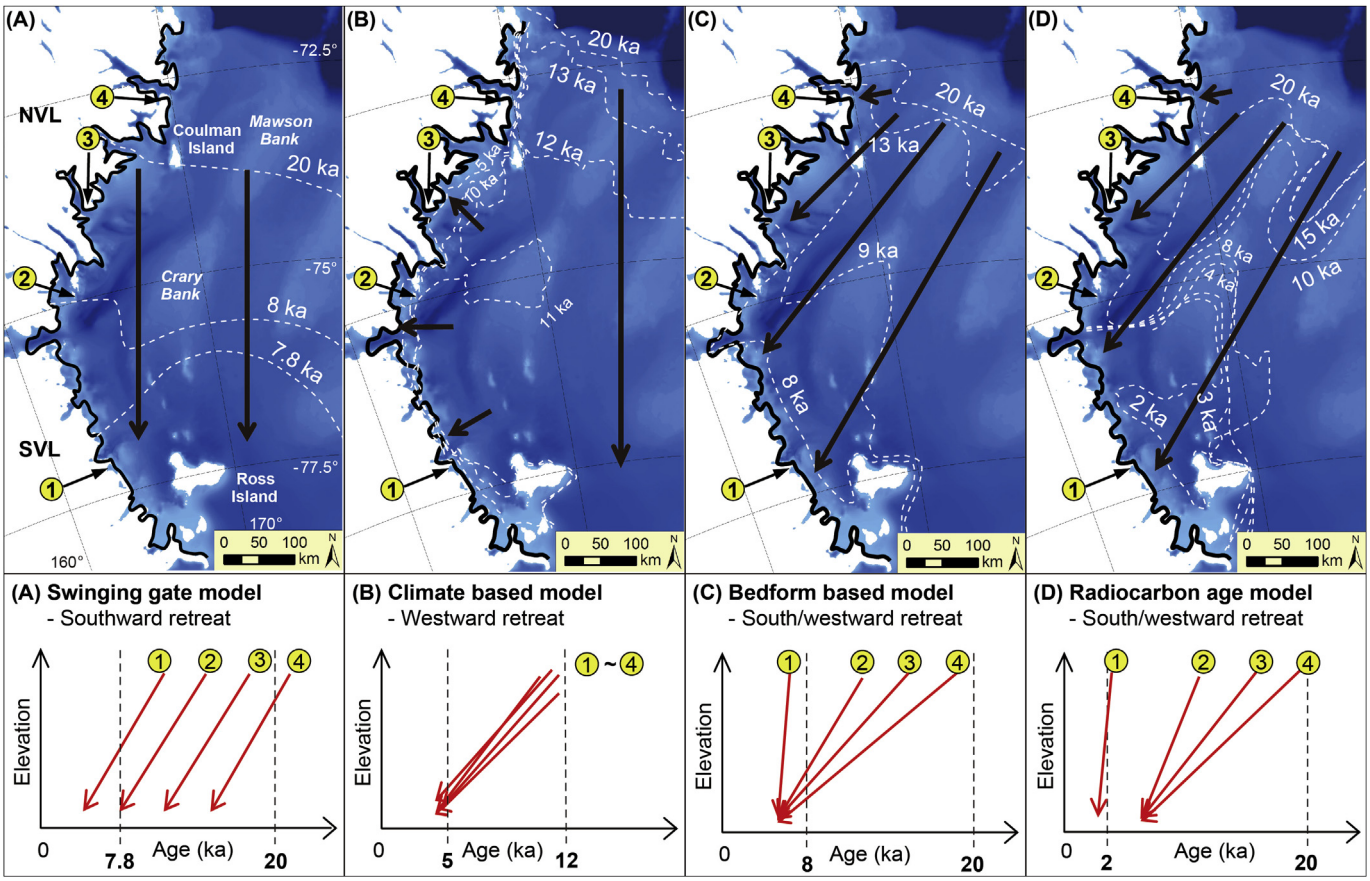

Fig. 9. Four hypotheses for the post-LGM retreat of the Ross Ice Shelf grounding line and the expected lowering reactions on the four studied Victoria Land outlet glaciers. The bold black line is the present-day grounding line, and the dashed white lines indicate the inferred pattern of grounding-line retreat for each hypothesis. (A) Swinging-gate model. The southward retreat of the grounding line should have exposed the glaciers to earlier open-marine conditions, inducing an earlier termination of deglaciation (Conway et al., 1999). (B) Climate-based model. The westward retreat of the grounding line should have produced a similar deglaciation period across the glaciers, as well as a similar lowering rate (Lowry et al., 2019). (C) Bedform-based model. The southwestward retreat of the grounding line is hypothesized to be due to major southward grounding-ice retreat and subsequent suspension of the outlet glaciers along the Victoria Land coast (Lee et al., 2017). (D) Radiocarbon-age model. This hypothesis has a similar grounding-line retreat pattern to that in (C), but the timeline of the southern grounding-line retreat is much later (Prothro et al., 2020). The bedform-based model in (C) provides the best match to the terrestrial observations of the spatiotemporal post-LGM deglaciation pattern along the Victoria Land coast.

stabilized on their mouths.

5.3. Horizontal changes in the Victoria Land outlet glaciers

We compared four Victoria Land outlet glaciers and found that the deglaciation trend terminated near 6 ka for each of the glaciers, whereas the onset of deglaciation varied along the Victoria Land coast, with an increasing delay in deglaciation to the south. The north-to-south onset ages of deglaciation for the four Victoria Land outlet glaciers are 17.2 ka (Figs. 7 and 8-④), 11.4 ka (Fig. 8-③), 8.9 ka (Fig. 8-②), and 6.8 ka (Fig. 8-①). This southward migration of glacier lowering indicates the approximate times when the glaciers encountered the southward migration of the Ross Ice Shelf grounding line and subsequent onset of an open marine condition (Fig. 8). Numerous studies have reconstructed the post-LGM Ross Ice Shelf grounding-line retreat, but the timing and pathway of this retreat are still debated (Conway et al., 1999; Ackert, 2008; Halberstadt et al., 2016; McKay et al., 2016; Lee et al., 2017; Lowry et al., 2019; Prothro et al., 2020). Models have considered mainly geological data (Fig. 9A; swinging-gate model), climatic forcings (Fig. 9B; climate-based model), subglacial geomorphological features (Fig. 9C; bedform-based model), and dating results from marine sediment cores (Fig. 9D; radiocarbon-age model). Here we consider which of these four major models best captures the observed terrestrial ice-thinning phases.

The most traditional "swinging-gate model" focuses on the retreat of the Western Antarctic Ice Sheet (WAIS) across the Ross Sea Embayment, with a limited supplement of ice from the EAIS (Conway et al., 1999, Fig. 9A). The glaciers draining into the western Ross Sea retreated southward, orthogonal to the Victoria Land coast since the retreat of the western Ross Sea ice occurred before the eastern Ross Sea ice retreated. The outlet glaciers along the Victoria Land coast may therefore have initiated surface lowering in a north-to-south sequence due to this southward migration of grounding-line retreat. The outlet glaciers in northern Victoria Land first encountered this grounding-line retreat and initiated deglaciation earlier than the outlet glaciers in southern Victoria Land. Deglaciation also terminated earlier along the northern outlet glaciers because the locally retreating grounding line approached its present-day grounding-line position and stagnated earlier. However, this pattern is not consistent with our observed deglaciation phases along the Victoria Land outlet glaciers, and there is also a timeline mismatch due to the limited ice-shelf extent at Coulman Island during the LGM (Halberstadt et al., 2016, Fig. 9A). The outlet of Tucker Glacier is also further to the north of Coulman Island, such that Tucker Glacier would have a limited effect on the ice-shelf variations in this model.

The "climate-based model" focuses on past ice-sheet retreat

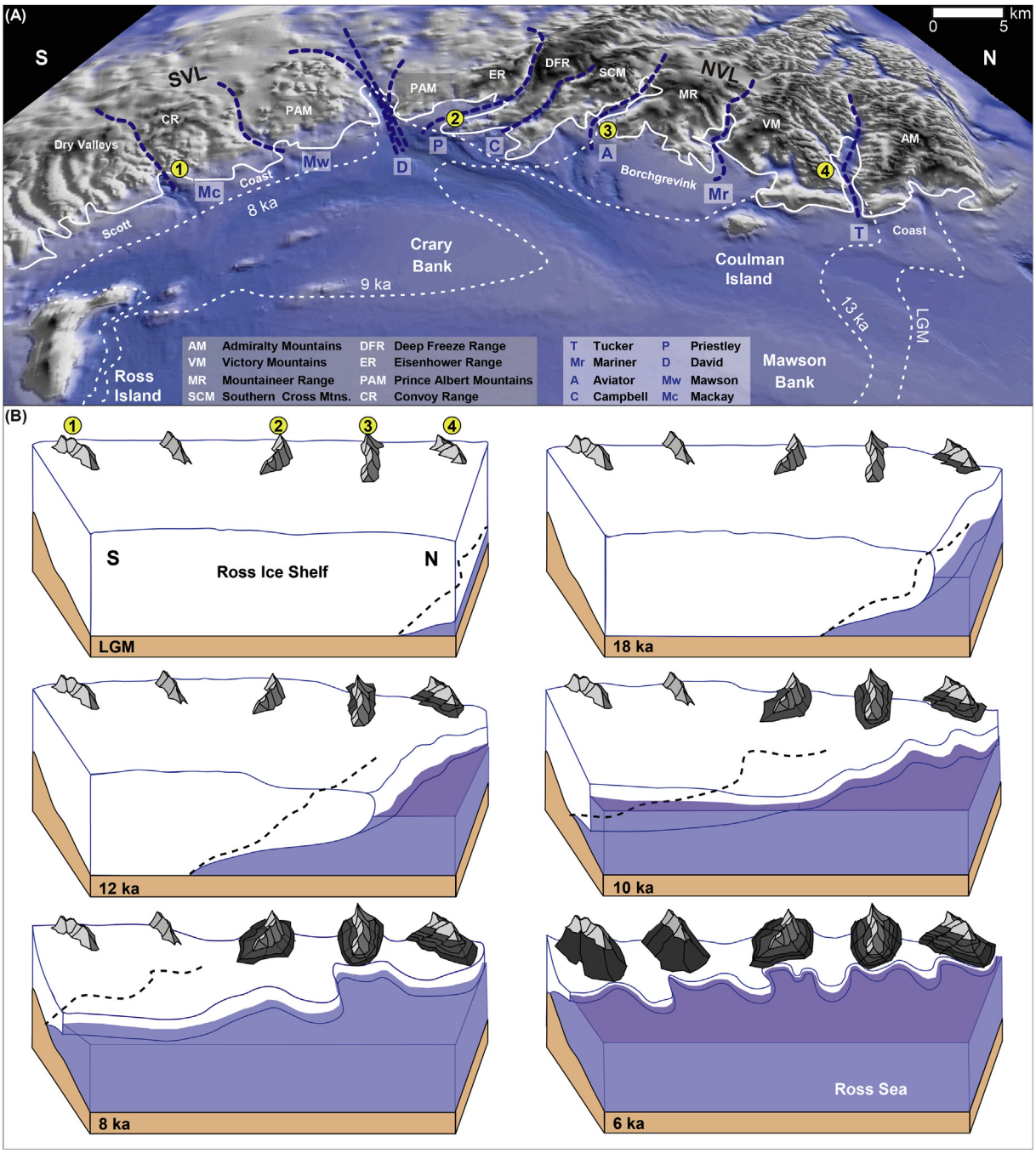

Fig. 10. 3D illustrated retreat/lowering of the Victoria Land outlet glaciers. (A) 3D hill-shaded topographic map along the Victoria Land coast. The dashed white lines indicate the grounding-line retreat of the Ross Ice Shelf based on marine bedforms (McKay et al., 2016; Lee et al., 2017). The bold white line indicates the present-day grounding line of the glaciers (Lowry et al., 2019), and the dashed blue lines are the major flowlines of the glaciers. (B) The terrestrial surfaces along the Victoria Land coast experienced different lowering rates of the outlet glaciers due to the southwestward migration of the palaeo-grounding line. (For interpretation of the references to color in this figure legend, the reader is referred to the Web version of this article.)

across the Ross Sea and considers atmosphere- and ocean-driven climate forcings using a fully coupled atmosphere–ocean general circulation model (Lowry et al., 2019, Fig. 9B). This model suggests that major, early grounding-line retreat appeared in the central embayment, with the ice discharged from the EAIS stagnating in the western Ross Sea due to delayed retreat. However, the modeled migration across the western Ross Sea during the Holocene indicates earlier retreat parallel to the Victoria Land coast, with minimal variations in glacier extent. This westward migration should have drained the outlet glaciers along the Victoria Land coast during a similar period and with a similar amount of lowering. However, the resolution and sensitivity of the deglaciation phase in the terrestrial and marine settings do not match well enough to explain their actual patterns, particularly since our study area is focused on a localized and marginal area of the Ross Sea.

The “bedform-based model” is based on a reconstruction of the subglacial basal geomorphology using multibeam bathymetry data and seismic profiles (McKay et al., 2016; Lee et al., 2017, Fig. 9C). It

was developed from the "saloon-door model" which found the thinner ice sheet on the central basin due to the thicker ice supplement on margins (Ackert, 2008), This model suggests that the first opening of the central basin of the Ross Sea occurred when the WAIS retreated. The western Ross Sea opened much later, with landward-migrating grounding-line retreat due to the influx of ice from the EAIS outlet glaciers. This influx of ice was so abundant that it was not deflected by ice flow from the central basin, resulting in stagnated ice loss along the Victoria Land coast, delayed grounding-line retreat, and ice surface drawdown. The grounding line retreated to the southwest, parallel to the Scott Coast along southern Victoria Land, with some curvature around Crary Bank, which obstructed further ice movement. The migration initiated ice thinning in the northern area before in the southern area, but the delayed stagnation along the Victoria Land coast unified the termination of deglaciation to a similar period and drawdown to a similar elevation.

The "radiocarbon-age model" uses compiled radiocarbon ages from sediment cores across the Ross Sea, to reconstruct the post-LGM evolution of grounding-line retreat (Prothro et al., 2020, Fig. 9D). The age results are compared with sediment facies to recover the timing of open-marine conditions and deposition proximal to the grounding line. The reconstructed pattern of the grounding-line retreat is similar to the "bedform-based model," with a southwestward migration. The timeline from LGM to >8 ka also appears reasonable compared to the actual grounding-line migration pattern. However, the grounding line stagnated on Crary Bank between 8 and 2 ka and led to a delay in open-marine conditions across the southwestern Ross Sea until 3 ka. The major lowering of Mackay glacier occurred occurred near 7–6 ka, whereas Crary Bank had limited any fluctuations in the grounding-line position until 3 ka. The major ice retreat along Mackay Glacier occurred between 3 ka and 2 ka, which does not align with the terrestrial deglaciation records.

The "bedform-based model" best fits our comparative terrestrial results of the post-LGM north-to-south migration of glacier lowering along the Victoria Lands coast (Figs. 9C & 10). The timing of grounding-line retreat (20–8 ka) also corresponds to the glacier lowering period (18–6 ka) along each outlet glacier, with the slight difference reflecting the lag time between the marine and terrestrial responses (Jones et al., 2015).

6. Conclusion

Our effective-exposure-age study of Priestley Glacier, coupled with the previous terrestrial-exposure-age results from other outlet glaciers along the Victoria Land coast and marine records from across the Ross Sea, revealed the post-LGM glacier dynamics of the western Ross Sea region. These terrestrial and marine records were difficult to link due to the lack of ice thinning data, such that their successive changes could not be aligned. However, recent exposure dating studies have provided important information on the post-LGM ice-thinning history of the Victoria Land outlet glaciers. Although there were lags between the terrestrial and marine timings of deglaciation, the compiled Victoria Land coastal data suggest that their post-LGM deglaciation trend is best explained when grounding-line retreat is considered.

We determined the deglaciation period and the lowering rate of Priestley Glacier at Inexpressible Island using the exposure age dating of erratic cobbles. Priestley Glacier underwent ~254 m of glacier lowering between 8.9 and 5.9 ka, at a lowering rate of ~0.09 m a^{-1}. Several Victoria Land outlet glaciers were compared to determine the mechanism that triggered deglaciation. Marine ice sheet instability caused by complex environments could explain the not too rapid, and not too steady lowering of the glacier. The synchronous culmination of glacier lowering and sea-level rise near 6 ka also supports this hypothesis. However, the ice along the western Ross Ice Shelf retreated asynchronously along the Victoria Land coast (north-to-south migration), with deglaciation terminating along all of the glaciers at *ca*. 6 ka. The southwestward post-LGM migration of the western Ross Ice Shelf would best account for the observed outlet glacier thinning patterns.

Author statement

HHR and YBS: fieldtrip, sample analysis, and writing the manuscript. MKL, JIL, and K-CY: fieldtrip and writing the manuscript. BYY: AMS measurement and analysis.

Declaration of competing interest

The authors declare that they have no known competing financial interests or personal relationships that could have appeared to influence the work reported in this paper.

Acknowledgments

This research is supported by the Korea Polar Research Institute (PE20180). We greatly thank Dr. Ara Jeong for her help with the early version of this manuscript. We were given lots of practical advice and much support from Dr. Jong Ik Lee of the Korea Polar Research Institute during the field trip.

References

Ackert, R., 2008. Swinging gate or Saloon doors: do we need a new model of Ross Sea deglaciation. In: Fifteenth West Antarctic Ice Sheet Meeting. Sterling, Virginia, pp. 8–11.
Balco, G., Stone, J.O., Lifton, N.A., Dunai, T.J., 2008. A complete and easily accessible means of calculating surface exposure ages or erosion rates from 10Be and 26Al measurements. Quat. Geochronol. 3, 174–195.
Balco, G., Schaefer, J.M., LARISSA Group., 2013. Exposure-age record of Holocene ice sheet and ice shelf change in the northeast Antarctic Peninsula. Quat. Sci. Rev. 59, 101–111.
Baroni, C., Hall, B.L., 2004. A new Holocene relative sea-level curve for Terra Nova Bay, Victoria land, Antarctica. J. Quat. Sci. 19, 377–396.
Baroni, C., Orombelli, G., 1991. Holocene raised beaches at Terra Nova Bay, Victoria land, Antarctica. Quat. Res. 36, 157–177.
Bentley, M.J., Hodgson, D.A., Smith, J.A., Cofaigh, OC., Domack, E.W., Larter, R.D., Roberts, S.J., Brachfeld, S., Leventer, A., Hjort, C., Hillenbrand, C-D., Evans, J., 2009. Mechanisms of Holocene palaeoenvironmental change in the Antarctic Peninsula region. Holocene 19, 51–69.
Berkman, P.A., Forman, S.L., 1996. Pre-bomb radiocarbon and the reservoir correction for calcareous marine species in the southern ocean. Geophys. Res. Lett. 23 (4), 363–366.
Clark, P.U., Dyke, A.S., Shakun, J.D., Carlson, A.E., Clark, J., Wohlfarth, B., Mitrovica, J.X., Hostetler, S.W., McCabe, A.M., 2009. The last glacial maximum. Science 325 (5941), 710–714.
Conway, H., Hall, B.L., Denton, G.H., Gades, A.M., Waddington, E.D., 1999. Past and future grounding-line retreat of the west antarctic ice sheet. Science 286, 280–283.
Cuffey, K.M., Clow, G.D., Steig, E.J., Buizert, C., Fudge, T.J., Koutnik, M., Waddington, E.D., Alley, R.B., Severinghaus, J.P., 2016. Deglacial temperature history of West Antarctica. Proc. Natl. Acad. Sci. Unit. States Am. 113, 14249–14254.
Di Nicola, L., Strasky, S., Schlüchter, C., Salvatore, M.C., Akçar, N., Kubik, P.W., Christl, M., Kasper, H.U., Wieler, R., Baroni, C., 2009. Multiple cosmogenic nuclides document complex Pleistocene exposure history of glacial drifts in Terra Nova Bay (northern Victoria Land, Antarctica). Quat. Res. 71, 83–92.
Frezzotti, M., Tabacco, I.E., Zirizzotti, A., 2000. Ice discharge of eastern Dome C drainage area, Antarctica, determined from airborne radar survey and satellite image analysis. J. Glaciol. 46, 253–264.
Goehring, B.M., Balco, G., Todd, C., Moening-Swanson, I., Nichols, K., 2019. Late-glacial grounding line retreat in the northern Ross Sea, Antarctica. Geology 47, 291–294.
Golledge, N.R., Menviel, L., Carter, L., Fogwill, C.J., England, M.H., Cortese, G., Levy, R.H., 2014. Antarctic contribution to meltwater pulse 1A from reduced Southern Ocean overturning. Nat. Commun. 5, 5107.
Gosse, J.C., Phillips, F.M., 2001. Terrestrial in situ cosmogenic nuclides: theory and application. Quat. Sci. Rev. 20, 1475–1560.

Halberstadt, A.R.W., Simkins, L.M., Greenwood, S.L., Anderson, J.B., 2016. Past ice-sheet behaviour: retreat scenarios and changing controls in the Ross Sea, Antarctica. Cryosphere 10, 1003–1020.
Heyman, J., Stroeven, A.P., Harbor, J.M., Caffee, M.W., 2011. Too young or too old: evaluating cosmogenic exposure dating based on an analysis of compiled boulder exposure ages. Earth Planet Sci. Lett. 302, 71–80.
Howat, I.M., Porter, C., Smith, B.E., Noh, M.-J., Morin, P., 2019. The reference elevation model of Antarctica. Cryosphere 13, 665–674.
Jeong, A., Lee, J.I., Seong, Y.B., Balco, G., Yoo, K.C., Yoon, H.I., Domack, E., Rhee, H.H., Yu, B.Y., 2018. Late Quaternary deglacial history across the Larsen B embayment, Antarctica. Quat. Sci. Rev. 189, 134–148.
Jones, R.S., Mackintosh, A.N., Norton, K.P., Golledge, N.R., Fogwill, C.J., Kubik, P.W., Christl, M., Greenwood, S.L., 2015. Rapid Holocene thinning of an East Antarctic outlet glacier driven by marine ice sheet instability. Nat. Commun. 6, 8910.
Jones, R.S., Small, D., Cahill, N., Bentley, M.J., Whitehouse, P.L., 2019. iceTEA: tools for plotting and analysing cosmogenic-nuclide surface-exposure data from former ice margins. Quat. Geochronol. 51, 72–86.
Kohl, C.P., Nishiizumi, K., 1992. Chemical isolation of quartz for measurement of in-situ-produced cosmogenic nuclides. Geochem. Cosmochim. Acta 56, 3583–3587.
Korschinek, G., Bergmaier, A., Faestermann, T., Gerstmann, U.C., Knie, K., Rugel, G., Wallner, A., Dillmann, I., Dollinger, G., Von Gostomski, C.L., Kossert, K., 2010. A new value for the half-life of 10Be by heavy-ion elastic recoil detection and liquid scintillation counting. Nucl. Instrum. Methods Phys. Res. Sect. B Beam Interact. Mater. Atoms 268, 187–191.
Lal, D., 1991. Cosmic ray labeling of erosion surfaces: in situ nuclide production rates and erosion models. Earth Planet Sci. Lett. 104, 424–439.
Lambeck, K., Rouby, H., Purcell, A., Sun, Y., Sambridge, M., 2014. sea level and global ice volumes from the last glacial maximum to the Holocene. Proc. Natl. Acad. Sci. Unit. States Am. 111, 15296–15303.
Lee, J.I., McKay, R.M., Golledge, N.R., Yoon, H.I., Yoo, K.C., Kim, H.J., Hong, J.K., 2017. Widespread persistence of expanded East Antarctic glaciers in the southwest Ross Sea during the last deglaciation. Geology 45, 403–406.
Lifton, N., Sato, T., Dunai, T.J., 2014. Scaling in situ cosmogenic nuclide production rates using analytical approximations to atmospheric cosmic-ray fluxes. Earth Planet Sci. Lett. 386, 149–160.
Lilly, K., Fink, D., Fabel, D., Lambeck, K., 2010. Pleistocene dynamics of the interior East Antarctic ice sheet. Geology 38, 703–706.
Lowry, D.P., Golledge, N.R., Bertler, N.A., Jones, R.S., McKay, R., 2019. Deglacial grounding-line retreat in the Ross Embayment, Antarctica, controlled by ocean and atmosphere forcing. Sci. Adv. 5, eaav8754.
McKay, R., Golledge, N.R., Maas, S., Naish, T., Levy, R., Dunbar, G., Kuhn, G., 2016. Antarctic marine ice-sheet retreat in the Ross Sea during the early Holocene. Geology 44, 7–10.
Nishiizumi, K., Imamura, M., Caffee, M.W., Southon, J.R., Finkel, R.C., McAninch, J., 2007. Absolute calibration of 10Be AMS standards. Nucl. Instrum. Methods Phys. Res. Sect. B Beam Interact. Mater. Atoms 258, 403–413.
Orombelli, G., 1989. Terra Nova Bay: a geographic overview. In: Ricci, C.A. (Ed.), Geosciences in Victoria Land, Antarctica. Memorie Della Società Geologica Italiana, vol. 32, pp. 69–75.
Owen, L.A., Caffee, M.C., Bovard, K.R., Finkel, R.C., Sharma, M.C., 2006. Terrestrial cosmogenic nuclide surface exposure dating of the oldest glacial successions in the Himalayan orogen: Ladakh Range, northern India. Geol. Soc. Am. Bull. 118, 383–392.
Parrenin, F., Masson-Delmotte, V., Köhler, P., Raynaud, D., Paillard, D., Schwander, J., Barbante, C., Landais, A., Wegner, A., Jouzel, J., 2013. Synchronous change of atmospheric CO2 and antarctic temperature during the last deglacial warming. Science 339, 1060–1063.
Prothro, L.O., Majewski, W., Yokoyama, Y., Simkins, L.M., Anderson, J.B., Yamane, M., Miyairi, Y., Ohkouchi, N., 2020. Timing and pathways of east Antarctic ice sheet retreat. Quat. Sci. Rev. 230, 106166.
Rhee, H.H., Lee, M.K., Seong, Y.B., Hong, S., Lee, J.I., Yoo, K.C., Yu, B.Y., 2019. Timing of the local last glacial maximum in Terra Nova Bay, Antarctica defined by cosmogenic dating. Quat. Sci. Rev. 221, 105897.
Rignot, E., Velicogna, I., van den Broeke, M.R., Monaghan, A., Lenaerts, J.T., 2011. Acceleration of the contribution of the Greenland and Antarctic ice sheets to sea level rise. Geophys. Res. Lett. 38, L05503.
Roberts, S.J., Hodgson, D.A., Bentley, M.J., Smith, J.A., Millar, I.L., Olive, V., Sugden, D.E., 2008. The Holocene history of George VI Ice Shelf, Antarctic Peninsula from clast-provenance analysis of epishelf lake sediments. Palaeogeogr. Palaeoclimatol. Palaeoecol. 259, 258–283.
Seong, Y.B., Dorn, R.I., Yu, B.Y., 2016. Evaluating the life expectancy of a desert pavement. Earth Sci. Rev. 162, 129–154.
Shepherd, A., Gilbert, L., Muir, A.S., Konrad, H., McMillan, M., Stater, T., Briggs, K.H., Sundal, A.V., Hogg, A.E., Engdahl, M.E., 2019. Trends in antarctic ice sheet elevation and mass. Geophys. Res. Lett. 46, 8174–8183.
Shepherd, A., the IMBIE team, 2018. Mass balance of the antractic ice sheet from 1992 to 2017. Nature 558, 219–222.
Stuiver, M., Reimer, P.J., 2000. Radiocarbon Calibration Program Calib Rev. 4.3. Quaternary Isotope Laboratory: University of Washington.
Sugden, D.E., Balco, G., Cowdery, S.G., Stone, J.O., Sass III, L.C., 2005. Selective glacial erosion and weathering zones in the coastal mountains of Marie Byrd Land, Antarctica. Geomorphology 67, 317–334.